Instabilities in Astrophysical Jets

M. Birkinshaw *
Department of Physics, University of Bristol, Tyndall Avenue, Bristol BS8 1TL, UK

Abstract. The observed properties of astrophysical jets are reviewed, and the techniques used to estimate the parameters of the underlying beams are described. This information is then used in a theoretical treatment of the Kelvin-Helmholtz instability of the flows, and the relevance of this instability to the persistence of the observed structures is emphasised.

Key words: Jets, Beams, Magnetohydrodynamics, Radio galaxies

1. Observed properties of astrophysical jets

I have chosen to start this review of astrophysical jet stability and instability by giving some of the essential observational background on real astronomical sources, and on the results of large-scale computer codes that attempt to explain what we are seeing in terms of a flow model. In later sections I will describe the methods used to try to get at the physical parameters of the beams that underlie the observed jets, and end with a discussion of the important issue of stability: whether the underlying beams can propagate to large distances without disrupting.

1.1. Introduction to jets: extragalactic, galactic

M 87 provided the first example of an astrophysical jet (Curtis, 1918). The detail that is visible in modern optical and radio images of M 87 (Biretta & Meisenheimer, 1993) reinforces the strong impression of *flow* that we get when looking at them: how else, it might reasonably be asked, can a linear structure exist in a chaotic object like an elliptical galaxy? However, the modern idea that quasi-continuous flows from the nuclei of elliptical galaxies may appear as jets of this type was not developed until the 1970s, when the idea that these jets trace the flow of matter and energy into the outer parts of radio galaxies (such as the radio lobes of Cygnus A; Section 1.2.2) was expounded and elaborated (Rees, 1971; Scheuer, 1974; Blandford & Rees, 1974).

Jets are now recognised as an important phenomenon in both extragalactic radio sources (such as M 87, Cygnus A, and NGC 6251) and galactic objects (such as SS 433, HH 34, and GRO J1655-40). We see jets with a wide range of linear sizes and luminosities, and believe that jets are a *common* attribute of energetic objects. I will not be discussing the origins of jets—but whatever the controlling mechanisms are, they are effective from stellar to quasar luminosities.

* Also Smithsonian Astrophysical Observatory, 60 Garden Street, Cambridge, MA 02138, USA

The theoretical description of jet flows cannot be divorced from the observational basis of the phenomena: the limitations of astronomical data are such that many of the fundamental physical parameters of jets are not known. Often this looseness in the data gives us too much theoretical freedom of maneuver, but conversely, a theoretical understanding of jet flows should help us to measure the physical parameters of these interesting astronomical objects.

It will help us avoid confusion if we carefully distinguish between *jets* and *beams* in what follows. I will always use the term *jet* to describe an astrophysical structure which looks as if it corresponds to a mostly-linear, collimated flow. It should always be remembered that what we see as a jet may only be loosely related to the underlying structure (see Section 2.1). I will use the term *beam* to refer to the underlying flow that is supposed to result in the observed jet. That is, the beam is the theoretical flow that is supposed to result in the observed jet structure. The beam model is now quite well accepted, but observational studies of jets continue to test it.

A good reference on the properties of astrophysical jets and their interpretation in terms of the beam model is Hughes (1991).

1.2. Observed structures of jets

The easiest way to explain what is meant by a jet is to show some examples. In this section I discuss some of the more famous jets, and recent data that shows how much more detail of jet structures we are beginning to see.

1.2.1. *M 87 (NGC 4486; 3C 274)*

Recent radio and optical images of the jet of M 87, which is one of the closest and best-studied extragalactic jets, appear in Biretta & Meisenheimer (1993). On the scale of a few kpc, we see a knotty, somewhat bent, jet which has an angular width that generally increases at increasing distance from the center of the galaxy, and which is embedded in a large-scale "halo" of diffuse emission. At low radio frequencies, and on large angular scales, the jet is inconspicuous: the steep-radio-spectrum emission from the halo has a higher apparent surface brightness. A detailed examination of the maps shows limb brightening in the regions between the knots (Owen *et al.*, 1989).

One attraction of the study of M 87 is that the galaxy is relatively nearby (in the Virgo cluster), so that arcsecond-scale resolution from ground-based optical telescopes and interferometers corresponds to physical structure with about 100 pc scales. The highest resolution imaging, from VLBI (e.g., Junor & Biretta 1995) shows jet-like structures on scales < 0.1 pc, continuing very close to the bright unresolved radio component associated with the core of the galaxy. A high quality VLBI map (Reid *et al.*, 1989) shows that M 87 contains a jet which is already very linear on the scale of a few pc.

Recent HST data (Ford *et al.*, 1994; Harms *et al.*, 1994) show that the centre of M 87 contains a disk of gas and dust, which is rotating at ~ 550 km s^{-1} only 20 pc from the centre of the galaxy. If this is interpreted as the Keplerian motion of cold material in the gravitational field of the nucleus, then the nucleus may contain a supermassive black hole, with mass $M \sim 3 \times 10^9\ M_\odot$. A favourite prejudice is that it is the presence of such objects that provides the ultimate (gravitational) energy source that powers the jet flow: however, I do not intend to discuss the question of the power source, or the initial generation of jets.

On the smallest (sub-milliarcsec) scales, the jet does not vary significantly with time: the pattern of emission knots and extended emission that is seen appears to be static, with $v < 0.05c$ (Junor & Biretta, 1995). On the milli-arcsec scale, bright knots in the jet are moving out from the most compact component in the source with speed $(0.28 \pm 0.08)c$ (Reid *et al.*, 1989). On the arcsec scale of the large-scale jet, the knots appear to be expanding from the core of the source with speeds of about $0.5c$, with some compact features in the knots moving at several c (Biretta & Meisenheimer, 1993). Clearly this is indicative of a relativistic phenomenon, but the interpretation of an apparently accelerating flow is unclear: is it the fluid that is moving relativistically and accelerating (and if so, how is the acceleration produced at distances of order 1 kpc from the nucleus of M 87)? Or is what we are seeing merely a pattern velocity, which may be moving much faster than the flow itself (see Section 2)?

The VLBI source is known to be variable on month time-scales (e.g., Morabito *et al.*, 1988). Such variability of brightness may correspond to variability of input of energy into the radio jet, although on the arcsecond-scale of the large jet, where the length scales are larger than in the VLBI jet, it is likely that these variations are somewhat smoothed out if they correspond to flow variations.

1.2.2. *Cygnus A (3C 405)*

The closest of the "classical double" radio sources is Cygnus A, 3C 405, with redshift $z = 0.0565$ (Figure 1). Its large scale structure is that of two bright, steep-spectrum, radio lobes, with prominent "hot spots" towards the outer edges of the lobes. Near the middle of the source lies a compact radio component with angular size < 1 arcsec, and a flat spectrum. With the excellent dynamic range that can be obtained with present-day imaging instruments, such as the VLA, and image processing techniques, the source can also be seen to posess faint linear features "jets" which form almost straight connections from the central component to the brightest parts of the source (Perley *et al.*, 1984b; Fig. 1). The NW jet is considerably brighter than the SE "counterjet". Both jets have length > 30 arcsec (50 kpc), so that they extend far from the center of the parent giant elliptical galaxy, and into the atmosphere of the poor(ish) cluster of galaxies that contains it (Arnaud *et al.*, 1984).

A close examination of the structure of the jets on Figure 1 shows that these are slightly misaligned, with the SE jet lying $7°$ to the south of the backward

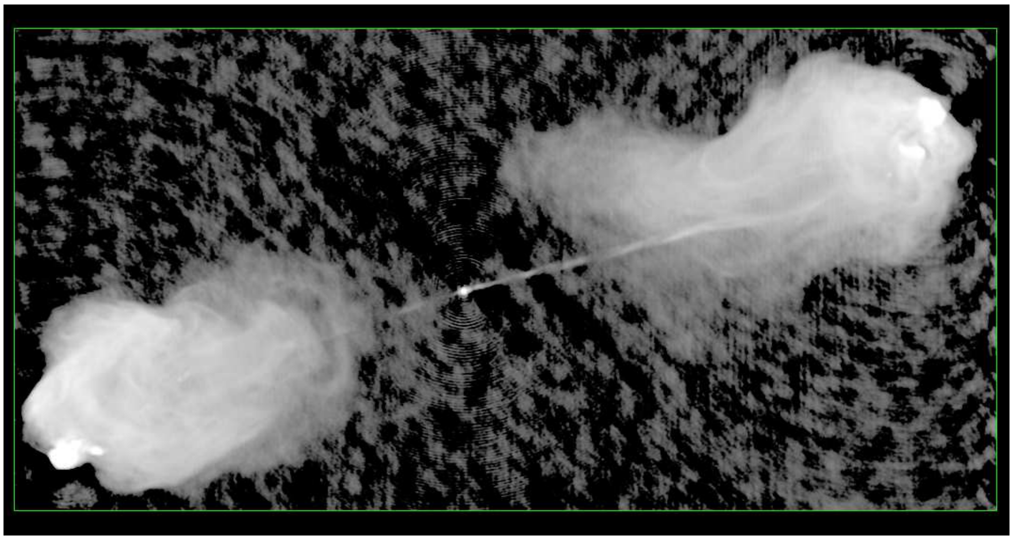

Fig. 1. A 6-cm radio image of Cygnus A, from the VLA, with a logarithmic grey-scale. The dominant features of this image are the two bright radio lobes to the NW and SE of the radio core, with their embedded hot spots, but this high dynamic range image also shows linear features extending from the core towards the brightest parts of the lobes. These features are the jet (oriented to the NW) and counter-jet (to the SE). Figure supplied by Chris Carilli, CfA.

extrapolation of the NW jet. The NW jet shows clear internal structures. Where it is clearly separated from the lobe, it shows several bright knots, which are themselves elongated almost along the line of the jet, but in fact inclined at about 6° to this line, and which appear at regular intervals of about 10 arcsec. About 30 arcsec from the core, the NW jet seems to split into two, and bend significantly, before it becomes lost against the bright lobe emission. Multifrequency maps show that the jet has a spectral index of 0.85 ± 0.20 (Carilli *et al.*, 1991), but that the knot closest to the core may have a steeper spectrum, with spectral index ~ 1.4.

At very high (milliarcsec) angular resolution, a small jet source is also seen in the central component: this jet is closely aligned with the NW jet (Linfield, 1985). The core is variable—about 15 per cent variability is seen over time scales of 1 to 2 years (Carilli *et al.*, 1991). This variability is presumably related to the high-speed, $(0.4 - 1)c$, motions seen in the VLBI (Carilli *et al.*, 1994).

One particularly interesting set of results from the mapping of Cygnus A relates to the polarization of the radio emission in the lobes (Dreher *et al.*, 1987). The polarization pattern reflects a magnetic field that traces the edge of the source and the bright "loops" of emission at high frequency, suggesting that magnetic fields are being sheared at the edge of the source and define the loop structures. At lower frequency, the effect of Faraday rotation (inside or outside the source) is to cause the polarization angle of the radiation to change. The amplitude of this rotation as a function of frequency is measured by the rotation measure, which can be mapped across the source and which measures the product of density and parallel (to the line of sight) magnetic field in the Faraday screen. For Cygnus A, huge rotation measures and rotation measure gradients are found. These are interpreted as evidence for magnetic field structures and density structures in the gas surrounding the lobe. A particularly sharp rotation measure feature, seen near one of the hot-spots in the NW lobe (Carilli *et al.*, 1988), is interpreted in terms of compressed gas and/or magnetic fields in the medium ahead of a strong shock.

A final element of the polarization data is the depolarization induced by magnetic fields and gas within the lobe. Differential Faraday rotation between the front and the back of the lobe will reduce the polarization below the value expected from the synchrotron formulae. It is difficult to disentangle this effect from the beam depolarization caused by the large rotation measure gradients, but it appears that the internal electron density in the lobes is less than about $3\times10^{-10}\ \mathrm{m}^{-3}$ (Dreher *et al.*, 1987) if the lobes are interpreted as containing a conventional electron/proton plasma.

1.2.3. *NGC 6251*

NGC 6251 is a relatively nearby ($z = 0.0243$) and apparently unexceptional elliptical galaxy which came to prominence in 1977, when Waggett *et al.* mapped it in the radio. The source has an overall angular size of ~ 1 deg and a generally double structure, with a central region containing an exceptionally clear-cut radio jet more than 4.5 arcmin (190 kpc, if in the plane of the sky) long. This jet has been well mapped by Perley *et al.* (1984a), and a low-frequency map of it is shown in Fig. 2 (Birkinshaw *et al.*, 1995). The radio spectra of all parts of the jet are remarkably similar, so that this 330-MHz map looks almost exactly like a 5-GHz map with the same resolution.

Within the radio core Cohen & Readhead (1979) found a bright one-sided jet that is almost aligned with the large-scale structure and which has an angular size of a few milliarcsec (about 2 pc) and a very small radius. No sign of the counterjet is apparent on the VLBI image, although a counterjet with a few per cent of the brightness of the main jet has been detected (Perley *et al.*, 1984a).

Returning to the larger scale, NGC 6251 has been mapped in the X-ray (Birkinshaw & Worrall, 1991) and shows itself to be dominated by a bright small-scale source (with angular size less than 15 arcsec), which may be associated with the active nucleus of the galaxy—either as non-thermal emission or as the X-radiation from a cooling inflow. However, this bright emission is surrounded by a faint halo of low surface brightness, which is interpreted as the X-ray emission of 90-kpc scale group gas.

Detailed maps of the jet show a radio polarization pattern that reflects a principally longitudinal field in the inner part of the jet. Further out the edges of the jet show a longitudinal field, while the centre of the jet shows a perpendicular field (Perley *et al.*, 1984a). The polarization from which this field pattern was inferred is generally high, so that there is no evidence for internal thermal material (which

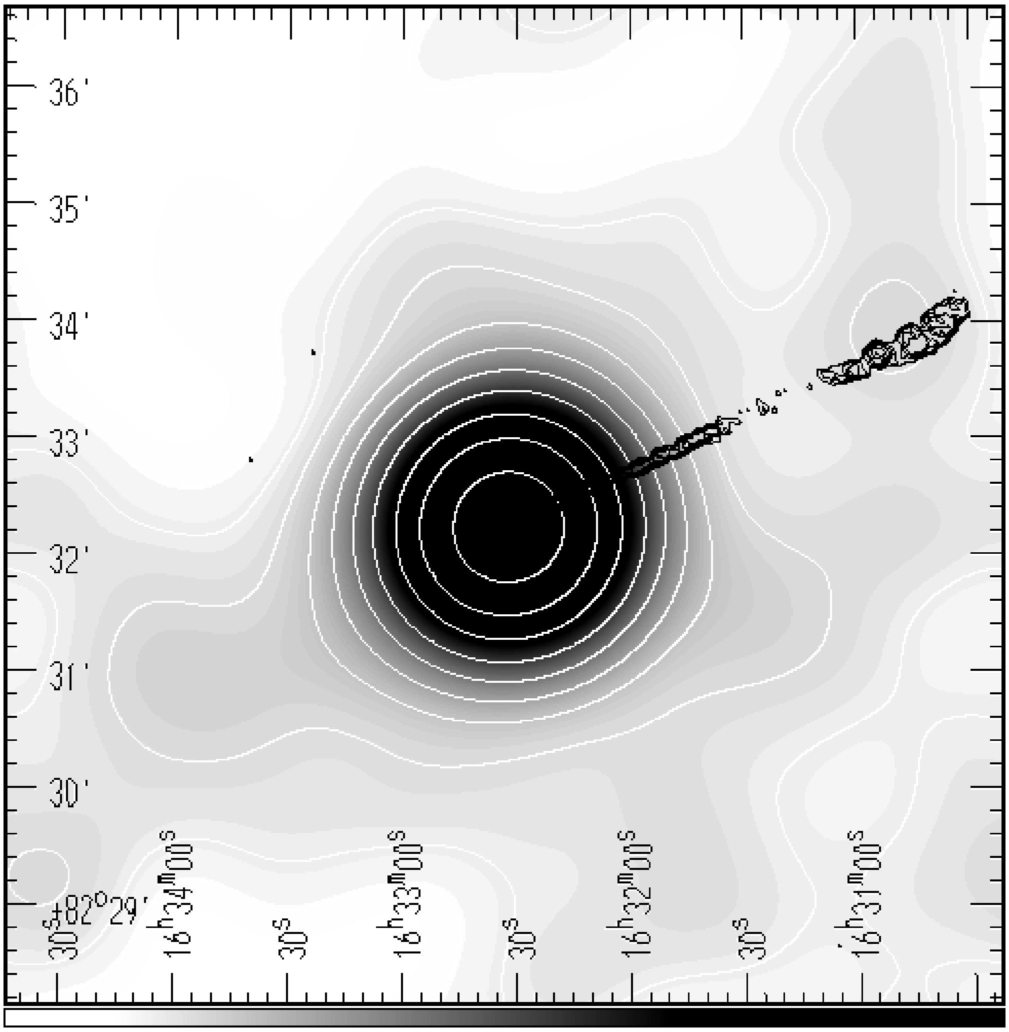

Fig. 2. A contour plot of a 330-MHz radio image of NGC 6251, from the VLA (Birkinshaw *et al.* 1995) superimposed on the ROSAT PSPC 0.2-2.4 keV X-ray image (Birkinshaw & Worrall 1993).

would cause a differential Faraday rotation between the front and back of the jet, and cause the polarization to fall), but the position angle of the polarization was found to show signs of a foreground Faraday screen in the inner part of the galaxy in the large Rotation Measure variations that it displays. The gradients of rotation measure are presumably caused by a lumpy material (in either density or magnetic field, or both) which appears superimposed on the jet.

If the usual minimum energy arguments are applied in this case, then the jet internal pressures are found to be well above the external pressure that can be provided by the X-ray emitting gas. This is, presumably, saying something about the way in which a radio source can affect the state of the surrounding medium—it is likely that the gas in direct contact with the jet has been shocked, and hence is at higher pressure than the general run of ambient gas. This also suggests that the radio source is non-static, since such a pressure imbalance implies that the source is changing structure on a sound crossing time in the ambient and jet gas.

1.2.4. *3C 449*

A 20-cm map of the inner part of 3C 449 appears in Perley *et al.* (1979), which is perhaps the paper that first demonstrated the effectiveness of the VLA for mapping radio jets. However, the source extends far beyond the well-mapped jet regions when mapped with higher surface brightness sensitivity, before terminating in low-surface brightness lobes. The inner jets show strong deflections, with the jet broadening significantly at about the location of the first major bends, and converting into plumes of emission that extend far beyond the optical galaxy. This is very unlike Cygnus A, for example, where the contrast between the jet brightness and the extended emission brightness is quite the other way round. Furthermore, 3C 449 shows nothing like the bright hot spots seen in Cygnus A.

These morphological differences between sources like 3C 449, which are fainter at the edge than in the centre, and Cygnus A, which is fainter at the centre than the edge, correspond well to radio power differences: 3C 449 has a radio power $P_{1\ \mathrm{GHz}} \sim 10^{25}\ \mathrm{W\,Hz^{-1}}$, whereas Cygnus A has a power $P_{1\ \mathrm{GHz}} \sim 10^{29}\ \mathrm{W\,Hz^{-1}}$. The morphology represented by 3C 449 is referred to as FR 1, and that represented by Cygnus A as FR 2, after the original description of the morphology/power correspondence by Fanaroff & Riley (1974).

1.2.5. *NGC 1265 (3C 83.1B)*

Lest you think that all radio jets are straight, consider the case of the FR 1 radio source 3C 83.1B, which is associated with NGC 1265 in the Perseus cluster (O'Dea & Owen, 1986). At low resolution the source appears to be a long trail of low surface-brightness radio emission, extending from the optical galaxy, which is located at the brightest part of the source. At higher resolution the brightest part of the source is seen to consist of two bright radio jets which emerge from a bright core roughly EW, and then curve to the north. Both jets are somewhat knotty, and end by expanding into large plumes that have the appearance of smoke trails seen from a factory chimney. The source is sometimes referred to as an example of a Narrow Angle Tail radio galaxy.

Very detailed mapping of the jets shows that they are brighter on their lower (convex) edges, and that the jets overlie lower-surface brightness emission with larger width but similar curvature. The centre lines of the jets "wiggle" from side to side about the smooth curvature that dominates. Polarization mapping suggests that the magnetic fields in the radio emitting plasma is predominantly aligned along the radio jets, at least in their inner parts (O'Dea & Owen, 1986). No strong spectral changes are seen over the jets, except that the knots are somewhat flatter than the extended emission.

1.2.6. *3C 273*

Extragalactic jets are seen in quasars as well as radio galaxies, with one of the best-studied being the quasar 3C 273 (Conway *et al.*, 1993). Although 3C 273 is somewhat special in showing both optical and X-ray jets in addition to the radio jet (Thomson *et al.*, 1993; Harris & Stern, 1987), the existence of the jet does make the point that there are some similarities in behaviour between radio galaxies and quasars. As seen in the Conway *et al.* radio map, the jet is around 80 kpc in projected size (its redshift $z = 0.158$). The general appearance of the jet is unlike the classical FR 1 or FR 2 jets and there is no detached hot spot of very high prominence. Instead the radio jet is of high surface brightness, which gradually increases towards the end. The core of the source is very bright relative to the jet.

Further information on the core is available from VLBI—3C 273 was the first source mapped with VLBI that showed definite evidence of superluminal expansion (at $v_{\rm app} \approx 8c$; for $H_0 = 50 \ {\rm km\,s^{-1}\,Mpc^{-1}}$; Pearson *et al.*, 1981), and hence relativistic flow on scales of a few pc.

1.2.7. *SS 433*

The star SS 433 was first reported as a bright Hα emission-line object. It is now realized that it is intensely interesting—it lies near the centre of the supernova remnant W 50, at a distance of 5 kpc, and displays prominent emission lines with a redshift which varies with a period of about 164 days. The amplitude of these variations corresponds to red- or blue-shifts of about 0.17 (see review by Margon 1984).

Such large redshifts force us to accept that relativistic ejection is taking place, and direct evidence for this ejection is available from radio mapping using the VLA and VLBI (Vermeulen *et al.*, 1993). Bright radio knots appear sporadically in the centre of the source, and move outwards at a speed of about 20 milliarcsec per day, brightening for about the first 10 days, and then fading in flux density. On the larger scale a continuation of this motion is seen (Hjellming & Johnston, 1988).

Both the motion of the individual radio brightness peaks and the periodic Doppler shifts are fitted well by a kinematic model in which blobs move out from the central source at a speed of $0.26c$. The direction of these ejections then precesses about an axis inclined at 79° to the line of sight, with the cone half-angle of the precession being about 20°. This causes the side-to-side wiggles in the locations of the blobs. The precession is driven by a binary companion, which has a 13 day period (seen in small Doppler shifts of the near-stationary line system).

The fact that a simple kinematic model for the radio peaks fits the structure on both the VLBI and VLA scales in SS 433 suggests that the ejected material

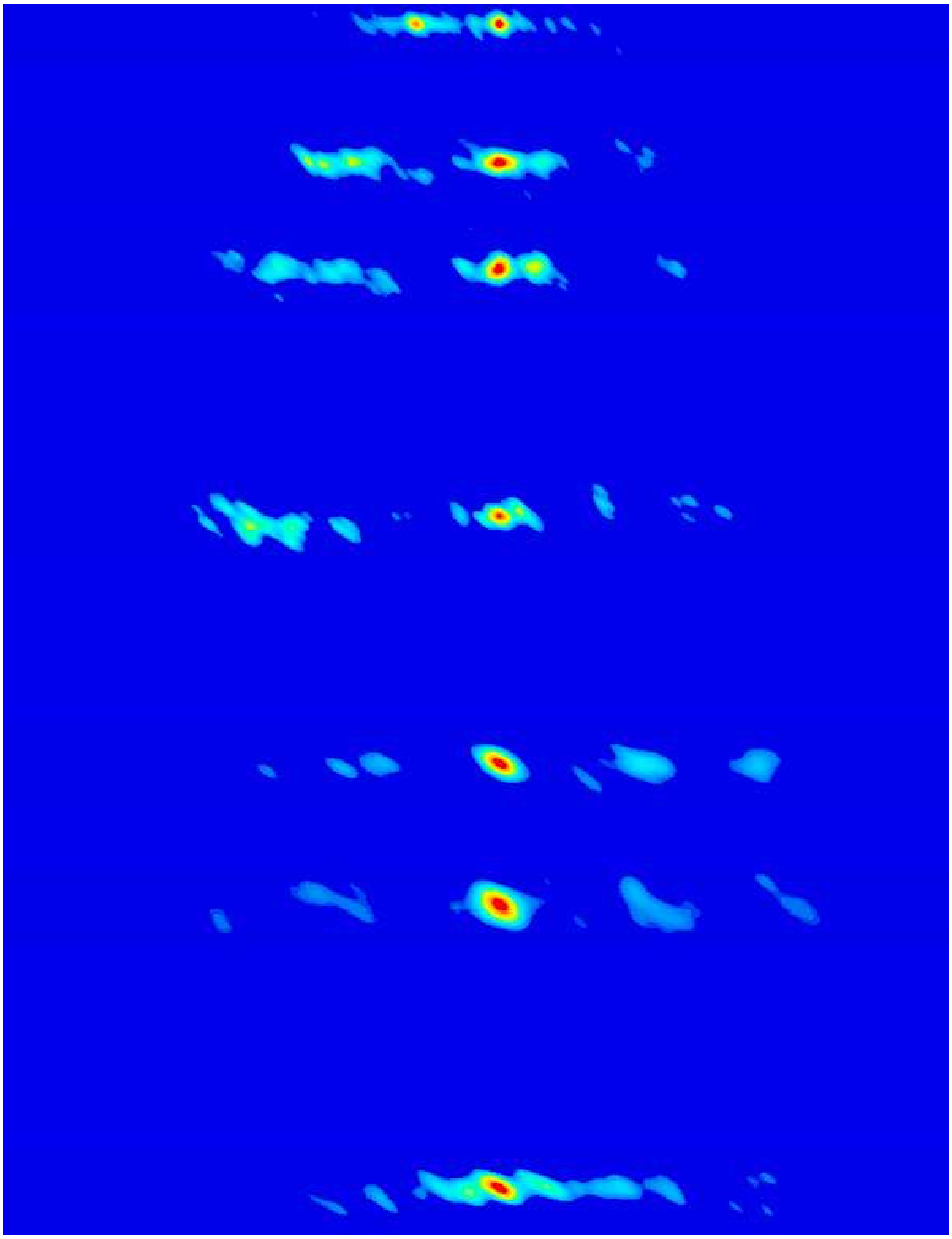

Fig. 3. The object GRO J1655-40, as imaged by the VLBA between Aug 18 and Sep 21, 1994 (Hjellming& Rupen 1995). The pattern of knots on either side of the core appears to expand at an almost constant rate: of 54 milliarcsec/day (on the NE side of the core) and 45 milliarcsec/day (on the SW of the core). At the distance of this object (about 3 kpc), this corresponds to a velocity of about $0.9c$.

is dense, and little affected by the properties of the gas through which it flows (the hot gas in W 50). An X-ray image of W 50 (Seward *et al.*, 1980; Watson *et al.*, 1983) shows enhanced X-ray emission from the neighbourhood of the jets and where the jets should hit the edge of W 50.

1.2.8. *GRO J1655-40*

The Compton Gamma Ray Observatory's Burst and Transient Source Experiment detected the X-ray source GRO J1655-40 on 27 July 1994. It was quickly found to be a strong radio source. When mapped with the Very Long Baseline Array (VLBA), it was seen to be a long, thin, jet-like object (Fig. 3; Hjellming & Rupen, 1995) which varied in both structure and flux density over over a period of a few days. As the source was followed for about a month, it became clear that several episodes of knot ejection from the core were occurring, at the times that the total radio flux density of the source flared. Hjellming & Rupen found that these knots are moving away from the nucleus at about 0.05 arcsec per day: at a distance of 3 kpc for GRO J1655-40, derived from the HI absorption spectrum, this corresponds to an apparent speed of about $0.9c$.

The appearance of the jet at different times (Fig. 3) clearly shows its asymmetry about the core of the source. It appears that individual ejection episodes cause bright blobs of radio-emitting plasma to appear near the core, and then to move away from the core at almost constant speed, suggesting a ballistic motion rather than conventional fluid flow. Thus GRO J1655-40 appears to be an extreme example of objects like SS 433: faster, but similarly shooting out dense blobs. The optical object is bright enough that detailed spectroscopy is possible: so far it has been shown that the parent object is a binary with about a 2.6 day period, and a mass function $\approx 3 M_\odot$ (Bailyn *et al.*, 1995a; Bailyn *et al.*, 1995b). A possible eclipse seen during optical monitoring (Bailyn *et al.*, 1995a) may cause any moving line system associated with the jet to be hard to see.

1.2.9. *HH 34*

It is not only energetic non-thermal objects that produce interesting jets. Star-forming regions also display jets. A well-known example is the HH 34 system. Herbig-Haro objects are bright, fuzzy, optical objects that appear on the dark backgrounds of molecular gas. They are thought to be a consequence of low-mass star formation, and frequently show high proper motions (a few hundred $\mathrm{km\,s^{-1}}$ being not unusual). HH 34 is a particularly spectacular optical jet (Reipurth *et al.*, 1986), which points back towards a star which is thought to be its source.

A recent HST image of HH 34 is shown in Fig. 4 (Hester *et al.*, 1995): we see a remarkably regular structure with distinct blobs of emission separated by a few hundred AU. Like the non-thermal sources SS 433 and GRO J1655-40, these blobs appear to be the results of distinct ejection episodes, "bullets" of high-speed gas that are shot out from the star. It is possible that there is a counter-jet of bullets on the other side of the star too, but these might be hidden by the dust and gas in

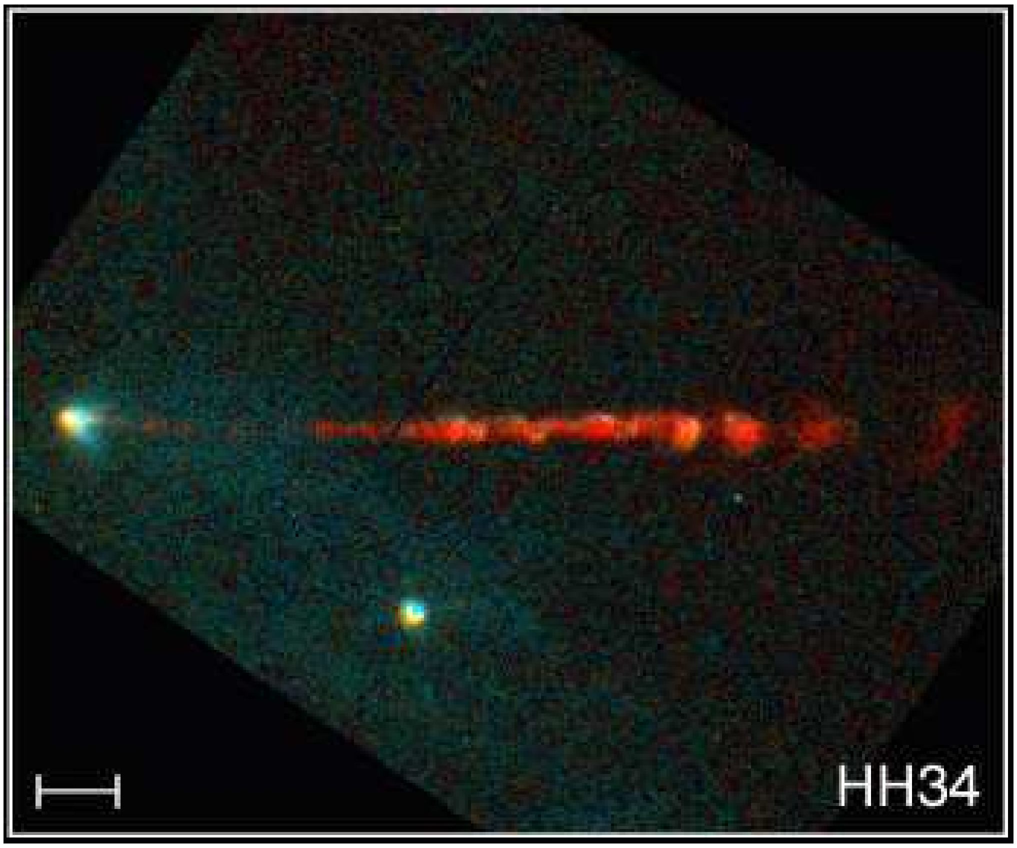

Fig. 4. The object HH34, as seen by the HST WFPC-2 camera (Hester *et al.* 1995). A regular series of knots is ejected from the originating stellar source to the left (North) of the image. The scale bar corresponds to 10^3 AU.

which the jet is embedded. The absence of a counterjet is a little unusual, though, since the visual absorption of the stellar source is only about 5 mag (Reipurth *et al.*, 1986), and it requires a somewhat special circumstances for one side of the jet to be exactly pointing out of the cloud while the other points into it.

The optical spectra of knots in the jet show emission lines that are produced by shocked gas and little or no continuum radiation. The knots are moving with a radial velocity of about -60 km s^{-1} relative to the parent star: once again we see evidence for motion, with a speed which is likely to be several times the sound speed in the medium in which it is embedded. The "head" of the flow, located well beyond the jet imaged by HST, is also moving rapidly relative to the core—and shows several distinct knots with significantly different radial velocities. Studies of the spectrum also suggest that the material emitting the line radiation has a density which is somewhat lower than that of the molecular gas near the jet: of course, this doesn't necessarily say anything about the non-radiating material, nor whether the jet is embedded in a locally lower-density medium.

In this case there is a second indication of motion, from CO observations which show the presence of a "bipolar flow" centered on the HH 34 jet (Chernin & Masson, 1995). Chernin & Masson's map of high-velocity molecular gas shows blueshifted material on the side where the jet lies and redshifted emission on the opposite side. The CO data can be used to estimate the mass and momentum in high-speed gas that has been generated by the star: it is found that roughly $0.003\ M_{\odot}$ is involved, and the momentum of the flow is about $0.006 M_{\odot}\,\mathrm{km\,s^{-1}}$. The jet is expected to be at least 10^4 years old (Bally & Devine, 1994), and it is plausible that the molecular outflow is material that has been accelerated by a beam of material from the star.

1.2.10. *L 1551*

Finally, another example of a molecular flow that has been associated with a jet, the L 1551 outflow. This was the first bipolar molecular outflow found, and remains one of the best studied. It is associated with the young stellar object IRS 5 and several Herbig-Haro objects. On the largest scale, molecular line observations have found redshifted and blueshifted high-velocity gas distributed in distinct lobes, each about 15 arcmin (0.7 pc) in size, lying on either side of IRS 5. The general structure of the source consists of two well-separated lobes of high-velocity gas seen in the ^{12}CO $J = 1 - 0$ line (Snell & Schloerb, 1985). At high resolution the brightest parts of the SW (blueshifted) lobe break up into a number of bright filaments that may represent hydrodynamical shocks (Barsony *et al.*, 1993).

Snell & Schloerb estimate the total mass of high-velocity gas to be about $0.9\ M_{\odot}$, and believe that it has been swept up by the expanding cavity that is defined by the lobes. The corresponding momentum is about $16\ M_{\odot}\,\mathrm{km\,s^{-1}}$ (Moriarty-Schieven & Snell, 1988).

The entire system appears to be being driven by IRS 5 which lies between the lobes, and which has a jet-line radio and optical appearance (Mundt & Fried, 1983; Rodriguez *et al.*, 1986; Fridlund & Liseau, 1994). Over a period of years, the knots in the IRS 5 optical structure have been seen to move apart, with an average tangiential velocity of about $180\ \mathrm{km\,s^{-1}}$, while optical spectroscopy (Stocke *et al.*, 1988) reveals radial velocities between -80 and $-290\ \mathrm{km\,s^{-1}}$ for the knots. Not all the knots are travelling in the same direction: the spread in directions is $\sim 20^{\circ}$. There is no clear pattern in the directions of motion: it is possible that the knot ejections have not been stable, although there is a pattern of one knot being ejected every 20 years (Fridlund & Liseau, 1994). The outflow momentum in the jets, calculated using knot masses estimated from their optical spectral lines, is much less than the momentum in the high-velocity molecular gas, which suggests that IRS 5 shows intermittent bursts of very high activity. Perhaps the jet seen today is the remnant of the last burst, or the precursor to the next.

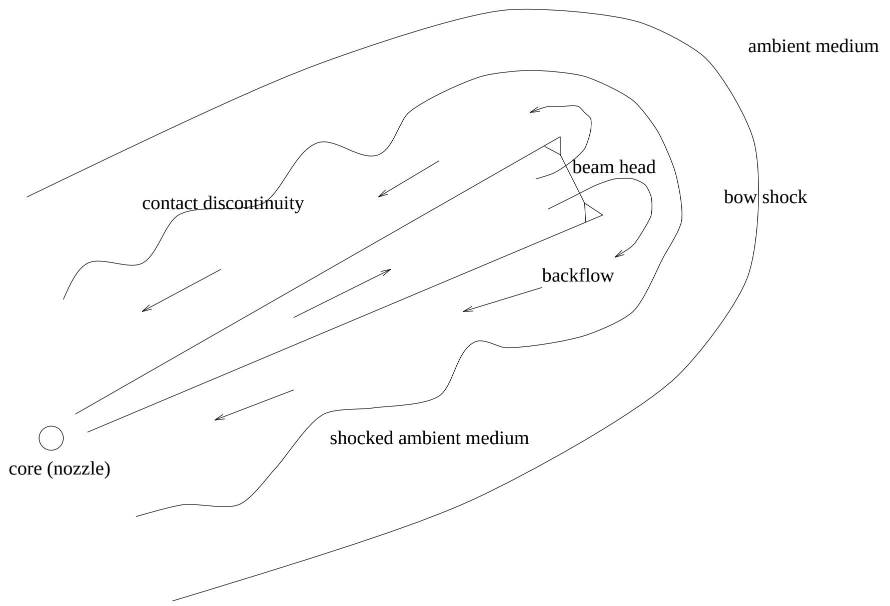

Fig. 5. A cartoon of a supersonic beam model, showing the most important features of the flow.

1.3. The beam model

So what are the characteristics of the beam model? In its simplest form, the idea is that the wide variety of jet structures that are seen can be attributed to the interactions of a collimated flow of gas (and magnetic fields) with the ambient gas through which it moves. A cartoon of a simple beam model, identifying the important segments of the flow, is shown in Fig. 5.

The initial injection of the beam is a difficult problem, for which there are a wide variety of models ranging from largely electromagnetic effects to largely gas-dynamical effects, such as the suggestion of a de Laval nozzle by Blandford & Rees (1974). In the context of the large-scale structures of jets that we are dealing with here, I shall ignore the important question of how a high-speed collimated flow is produced and simply examine how it propagates. Thus the beginning of the beam model for us will be where the flow exits some nozzle and comes into contact with the surrounding gas.

Assuming that the beam is supersonic, it will drive a shock into the ambient gas in front of the head of the beam. This bow shock compresses, heats, and accelerates the ambient medium. Material flowing down the beam leaves the collimated flow through a shock at the head of the beam, where it becomes much hotter (and hence highly over-pressured) and encounters the shocked ambient medium. In the rest-frame of the beam head, a circulation pattern is set up where the beam fluid expands into a backflow parallel to the beam. The interface between the rapidly-backflowing beam material and the shocked ambient medium is the contact discontinuity.

Since the velocities of the shocked ambient gas and the backflowing beam material are very different, there is the potential for creating strong Kelvin-Helmholtz instabilities at the contact discontinuity. The contact discontinuity may even be erased entirely. The interface between the beam and the backflowing gas provides another site where this instability might be active: and it was long thought that this instability would have a severe effect on the properties of the jet, destroying the collimated flow and hence preventing the creation of well-developed structures.

If the beam material can radiate energy efficiently, then compressions provide sites where substantial energy loss can take place and the flow can be severely modified (as it is expected to be in galactic jets). In extragalactic jets, where the energy loss is expected to be less significant, the beam head shock serves as a site at which particle acceleration can take place (Drury, 1983; Blandford & Eichler, 1987), and hence where synchrotron radiation might be possible. The beam head is therefore identified with the hot spots in FR 2 radio galaxies.

Further shocks can be created in the beams themselves, either as they pass through the structured cocoon that they have created, or because the injection mechanism is not completely steady. The latter suggestion has been used in the case of M 87, for example, to explain the prominent knots, and it is clear from some of the galactic jets (such as SS 433 and HH 34) that the unsteady injection of material is common on the stellar scale.

How about the FR 1 galaxies, which have no hot-spots? Here we can modify the previous picture by suggesting that the flows are not strongly supersonic, but transsonic or, perhaps subsonic. Then there is no strong shock at the head of the beam, and it is likely that the flow will be less well collimated and more likely to be distorted by disturbances in the ambient medium. In this context we can see a possible explanation for the very distorted jet in NGC 1265: it is likely that a beam emerging from the nucleus of this galaxy is being swept back by the ram-pressure of the ambient medium through which the galaxy is moving (Begelman *et al.*, 1994). NGC 1265 is a particularly good case for this explanation: it is located on the edge of the Perseus cluster, and has an anomalously high radial velocity relative to the systemic velocity of the cluster.

And what about the magnetic fields? If the fields are strong, then it is possible that they might dominate the flow: perhaps helping to collimate the beam (if circumferential), perhaps "guiding" the beam (if axial). If the fields are weak, then they will be dragged around by the flow, being sheared in some regions and tangled in others. But understanding the field structures is difficult in the abstract, and it is better to turn to full calculation to extract the details of the flow in particular cases.

1.4. Numerical models

Perhaps the most convincing evidence that we can understand the details of jets structure by a flow model is to examine numerical simulations of these flows. These simulations seek to solve the equations of gas-dynamics (or magneto-gas-dynamics, in the more adventurous codes) using computer models. Two cases are generally considered:

– adiabatic flows, where radiation from the beam is not significant in the evolution of the flow, and

– radiative flows, where the beam loses energy rapidly, through some radiation process.

Adiabatic flows are generally used to model extragalactic jets, since the physics involving the acceleration and transport of the relativistic particles that radiate energy is difficult, and it is expected that the observed radiation is only a small fraction of the kinetic luminosity of the beam. Radiative flows are used for the jets seen in star-forming regions, where the integrated radiation is a major coolant for the flow.

1.4.1. *Hypersonic, adiabatic flow*

Recent work by Loken *et al.* (1992) and Cioffi & Blondin (1992) considered the flow of a beam with very high speed and low density in a uniform ambient medium. Loken *et al.*'s 2D calculation involved a beam with density 0.01 of the ambient density, and a velocity 4650 times the sound speed in the ambient medium. The resulting flow pattern consists of a coherent high-speed beam, with a narrow forward-flowing cocoon next to the beam, a wider backward-flowing cocoon further out, then a further forward-flowing cocoon layer which is in contact with ambient gas which has passed through the bow shock. At the head, the beam material flows through a Mach disk into the cocoon, where it expands into a very low density medium which contains a complicated pattern of eddies. The beam itself carries significant density and pressure oscillations, and the beam head advances at a variable speed as the area of the head of the beam varies.

What does this tell us? It says that very fast, low density, flows can remain coherent as they propagate very many jet radii (more than 100 in this simulation), and that the cocoon that they inflate around themselves can be strongly overpressured relative to the external medium. This is of interest because the apparent pressures within many jets (e.g., NGC 6251) are higher than the pressures in the X-ray emitting gas through which they move. The simulation by Loken *et al.* assures us that it is not the original pressure of the ambient gas that keeps the beam from expanding dramatically, but the pressure of the self-generated cocoon of shock-heated gas, which is itself expanding into the intergalactic medium.

1.4.2. *Supersonic, adiabatic flows*

A typical ambient medium is intracluster gas around a radio galaxy, with a sound speed $\approx 1000\ \mathrm{km\,s^{-1}}$, so that the calculation by Loken *et al.* (1992) was certainly of a relativistic beam that cannot consistently be treated by non-relativistic gas-dynamics. However, it is generally agreed that the existence of compact hot-spots in FR II sources is probably due to the presence of a strong shock at the end of a supersonic jet, so this is a particularly interesting case to consider.

Many authors have discussed the propagation of supersonic jets (e.g., Norman *et al.* 1982; Williams & Gull 1985; Hardee & Clarke 1992; see the review by Williams 1991). As indicated by the cartoon of Fig. 5, the jets inflate a substantial cocoon about themselves, with a very low density backflowing material in contact with the beam. Strong waves can be seen in the contact discontinuity: these are driven by oscillations in the development of the beam head, but are likely to be maintained and amplified by the Kelvin-Helmoltz instability and (especially in 2-D simulations) by vortical flow at the injection plane and the beam-head.

1.4.3. *Subsonic, adiabatic flows*

As the speed of the flow drops, so the width of the insulating cocoon around the jet decreases. Williams (1991) shows a representative calculation in this case. The principal difference from the supersonic, adiabatic flows is that the beam is now in direct contact with the ambient gas. There is no bow shock, and the ambient material can flow fairly smoothly into contact with the beam around the plume of material that develops at the head of the flow. The pressure enhancement at the head is also small, so that there is no particular reason to expect a strong hot-spot. This type of flow may be a good model for FR 1 radio galaxies—the slower speed also makes them susceptible to environmental disturbances, which may help to bend them into some of the shapes that are seen.

1.4.4. *Supersonic, radiative flow*

The effect that radiative losses can have on a supersonic jet flow is well illustrated by the simulations of Blondin *et al.* (1990) and Gouveia Dal Pino & Benz (1993). As might be expected, compressions of the gas (especially in the beam) cause a rapid energy loss through radiation, so that the beam tends to be strongly compressed by the ambient medium, and a cold, dense shell of material tends to form at the head of the beam (Fig. 6). This shell of material is very unstable, and breaks into distinct clumps and (for some beams) a dense plug of material that is advected with the flow. The dispersing dense shell bears some resemblance to the complicated patterns of knots seen in Herbig-Haro objects, and displays something of the wide range of velocities that these knots show.

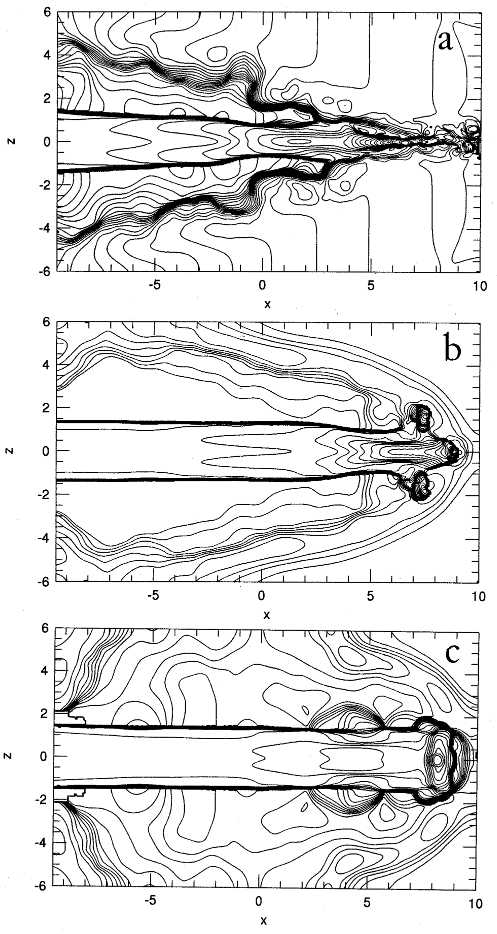

Fig. 6. The density structure of a radiative beam with initial density 3 times greater than the density of the ambient medium and Mach number $\mathcal{M}_a = 24$ after propagating into an ambient medium with increasing external density (a), constant external density (b), and decreasing external density (c). From Gouveia Dal Pino *et al.*, (1995).

1.4.5. *More complicated flows*

Most of the simulations in the past have considered the propagation of simple gas-dynamical beams through a uniform medium. With the continuing improvements in computer power, many more complicated calculations are now being done. For example, Hardee *et al.* (1992) considered the propagation of a slab jet through a medium with a temperature and pressure structure: Gouveia Dal Pino *et al.* (1995) have redone this calculation with a radiative flow in three dimensions (Fig. 6), finding a number of structural effects that are amplified by the presence of pressure gradients. There have also been a number of calculations of the effect on a beam of crossing a sudden jump in density or pressure, such as may be encountered as a beam crosses a shock front between the interstellar and intergalactic medium (e.g., Wiita *et al.* 1990, Wiita & Norman 1992). Balsara & Norman (1992) have repeated the analysis by Williams & Gull (1984) of the ram-pressure distortion of NGC 1265's jet, elucidating many of the structures in the deformed jet. De Young (1991) has studied cloud-jet interactions, finding dramatic structural changes which may be relevant to the wide angle tail radio galaxies (such as 3C 465; Leahy 1984) or double hot-spot objects. There has also been progress on flows containing dynamically-significant magnetic fields (e.g., Clarke *et al.* 1986b), although many of the resulting flows look rather unlike most radio jets.

2. Jet parameters

In Section 1 some of the general observational properties of (principally radio) jets were discussed. In the present Section, I will describe the essence of the methods that have been used to extract the properties of the underlying flow from these data. In other words, I am going to attempt to move from the "jet" to the "beam". I will concentrate on the extragalactic jets, for which the emission has a synchrotron origin, although the non-thermal galactic jets (associated with SS 433 and GRO 1655-40, for example) may be understood in the same way.

The properties of thermal galactic jets are studied principally through their line spectra, although thermal continuum is also seen. Line diagnostics of the density and temperature of the line-emitting region, and velocity information from proper motions and line shapes and centres, provide an extensive set of data for the galactic jets which helps to set their parameters more clearly than is possible for extragalactic jets.

2.1. Jet visualization

What are we seeing in the views of extragalactic jets. The high brightness of the radiation, and the polarization, imply that we see the jets through their radio synchrotron radiation. The jets may account for either a small (as in Cyg A) or a large (as in 3C 449) part of the overall energy radiated from the sources.

How is the radiation pattern that we see related to the material that is emitting? In synchrotron jets, the radiation is coming from ultrarelativistic electrons, with energy $E_{\rm e} \gg m_{\rm e}c^2$, moving in a magnetic field, of strength B. The effect of the field is to cause the electrons to circulate with frequency $\nu_{\rm g}/\gamma_{\rm e}$, where $\gamma_{\rm e} = E_{\rm e}/m_{\rm e}c^2$ and $\nu_{\rm g}$ is the electron gyrofrequency

$$\nu_{\rm g} = \frac{e\,B}{2\pi\, m_{\rm e}}. \tag{1}$$

The total power radiated by an electron is

$$P_{\rm tot} = 2\,\sigma_{\rm T}\,c\,\gamma_{\rm e}^2\,u_{\rm B}\,\sin^2\psi \tag{2}$$

where $\sigma_{\rm T}$ is the Thomson cross-section, $u_{\rm B} = B^2/2\mu_0$ is the magnetic energy density, and ψ is the pitch angle of the particle's motion about the magnetic field line on which it moves. The energy at which this radiation is produced lies in a fairly narrow band (compared to the wide frequency range of synchrotron radiation) about the critical frequency

$$\nu_{\rm crit} = \frac{3}{2}\gamma_{\rm e}^2\,\nu_{\rm g}\,\sin\psi \tag{3}$$

where the leading factor of $\gamma_{\rm e}^2$ arises because the radiation is beamed into the direction of motion of the radiating electron (as seen in the observer's frame), and because the motion of the electron about the field line causes this beamed radiation pattern to be pulsed into the line of sight of the observer only for a short fraction of each gyration. We can also estimate the radiative lifetime of an electron, the time taken to radiate a large fraction of its energy, $\tau_{\rm e} \approx E/P_{\rm tot}$.

If we now consider an ensemble of electrons, with an isotropic distribution of pitch angles (as is expected in radio jets), and a number per unit volume described by a power-law energy distribution

$$n(E)dE = n_{\rm E}\,E^{-\gamma}dE \tag{4}$$

with $E_{\rm L} < E < E_{\rm U}$, the averaged emission coefficient of the population of electrons is

$$j_\nu = \Lambda_{\rm j}\,N_{\rm e}\,(B\,\sin\theta)^{\alpha+1}\left(\frac{\nu}{c_\nu}\right)^{-\alpha} \tag{5}$$

where Λ_1 is a pure number which depends on α, θ is the angle between the magnetic field vector $\mathbf{B}$, and the line of sight, $c_\nu = 3e/4\pi m_{\rm e}^3 c^4$, and the spectral index,

$$\alpha = \frac{\gamma - 1}{2}. \tag{6}$$

(5) applies only in the range of frequencies for which the radiating electrons have energies $E_{\rm L} \ll E \ll E_{\rm U}$. Above and below this band, the spectrum turns down. Examples of broad-band spectra with synchrotron fits are shown in Fig. 7.

If we assume that the radio jets that we observe are optically thin (as is usually the case), then the radio brightness at the surface of the jet is

$$I_\nu = \int_{-\infty}^{\infty} j_\nu\,ds. \tag{7}$$

so that the observable flux density from a radio jet is determined by the mix of magnetic field strengths, magnetic field orientations, and electron spectra along the line of sight. Thus variations in the brightness of a radio jet may reflect variations in the number of relativistic electrons per unit volume, variations in the magnetic field strength or its direction, changes in the fraction of the jet width that is

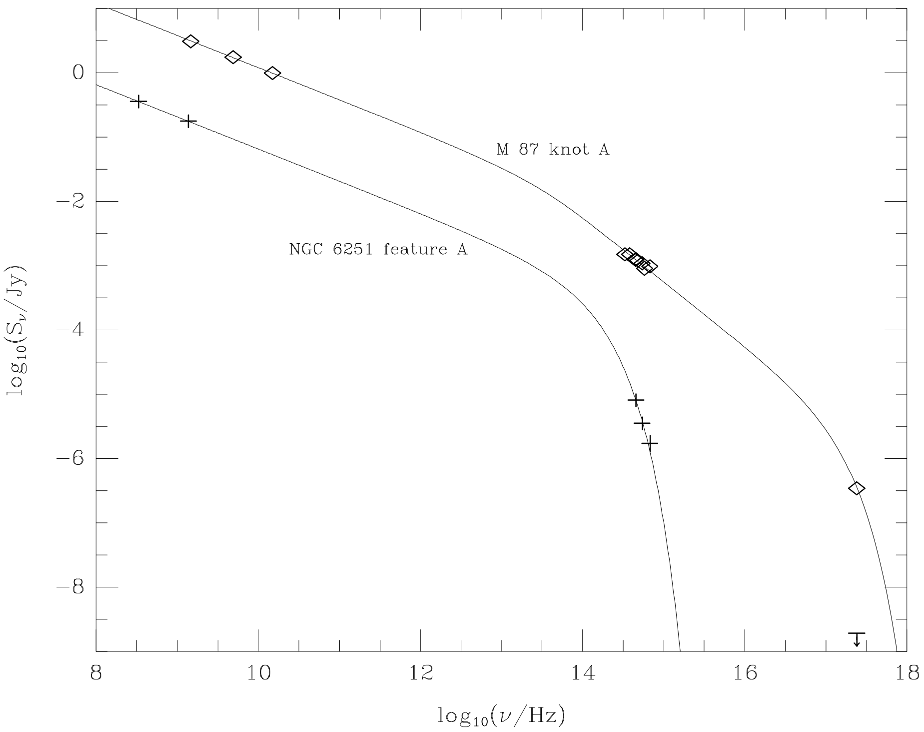

Fig. 7. The radio to X-ray spectra of feature A in NGC 6251 (crosses and upper limit) and knot A in M 87 (diamonds), from Birkinshaw & Worrall (1991). For most of these points the errors are smaller than the sizes of the symbols. The solid lines represent rough fits to these spectra from the synchrotron emission of optically-thin model electron energy distribution functions. The fit for NGC 6251 feature A is based on a simple power-law electron energy distribution that is cut off at energies $E > E_{\rm U}$, while the model distribution for M 87 knot A also posesses a break of unity in the electron energy index (and hence a break of 0.5 in the photon spectrum) at intermediate energy $0.02 E_{\rm U}$, which may be related to electron ageing, although the location and size of the break are poorly constrained. Neither spectrum shows any sign of a turn-down at low energies due to a lower energy cutoff of the electron spectrum.

occupied by radiating plasma, or all of these. Unique inversion of synchrotron data to obtain an accurate internal structure for a jet will clearly be difficult!

Some additional clues about the structure in the magnetic field within a jet can be gained through studies of the polarization. Within the frequency range that the spectrum appears power-law (i.e., the optically-thin regime between the frequency limits), the fractional linear polarization of the emission is

$$\Pi_{\rm L} = \frac{\alpha + 1}{\alpha + \frac{5}{3}} \tag{8}$$

which for sources with typical spectral indices, $\alpha \approx 0.5$, leads to a polarization of about 70 per cent. If the magnetic field is structured on the line of sight through a synchrotron plasma, the polarization can be dramatically reduced. If magnetic field lines viewed along the line of sight have a random orientation about that line of sight, the polarization will drop to zero (provided that the relativistic electron population in each region of magnetic field is the same). If the magnetic field lies in a single direction, but with many reversals, then the polarization will be at the value given by (8), since the polarization is independent of field *sense*. Laing (1980) and Hughes (1985) give more details on this *structural depolarization*.

In view of this effect, the large fractional linear polarizations seen in many jets (e.g., in M 87) indicate that the magnetic fields in the regions that are radiating are at least partially ordered and that there are not many random cells of magnetic field along the line of sight. Of course, this only relates to the regions where the relativistic electrons are concentrated: if the electrons can diffuse freely across the field lines, then this is a strong statement about the magnetic field structure over the entire jet. If the electrons cannot diffuse freely, or have radiative lifetimes which are small compared with the time taken to diffuse across the jet, then it is possible that we see only a small sample of the magnetic field structure of a jet in each polarization measurement.

The apparent polarization structure of a radio jet is also affected by Faraday rotation and Faraday depolarization. When a linearly polarized radio wave travels through a medium containing non-relativistic electrons and magnetic field, the fractional polarization remains unaltered, but the plane of polarization rotates by an angle

$$\chi = \mathcal{R}\,\lambda^2 \tag{9}$$

where the rotation measure

$$\mathcal{R} \propto n_{\mathrm{e,th}}\, B_{||} \tag{10}$$

with $n_{\mathrm{e,th}}$ being the thermal electron density and $B_{||}$ the component of the magnetic field associated with this thermal electron population and parallel to the line of sight. This means that if a radio jet, with a high fractional polarization, is located behind a screen containing magnetic field and electrons, the apparent position angle of the polarized flux will change as the wavelength of observation changes. At very short wavelengths, χ will be small and the plane of polarization indicates the intrinsic electric vector of radio waves emitted in the source. The magnetic field in the source is then 90° from the direction of the electric vector. Polarization maps in the literature are usually corrected for Faraday rotation as measured from multi-wavelength data and corrected to zero wavelength using (9).

More insidious is the possibility that thermal electrons are mixed with relativistic electrons in the radio source itself. Then the phenomenon of Faraday depolarization can arise: radiation from the rear of the jet and from the front of the jet pass through different amounts of thermal material, and therefore show different Faraday rotations. This means that the apparent degree of polarization of the radiation is reduced below the expected fraction (8). The wavelength-dependence of the effect can then produce a variety of patterns of variation in the apparent linear polarization fraction as a function of frequency (e.g., Cioffi & Jones 1980; Laing 1984). Relativistic electrons in the beam plasma are much less effective at producing Faraday rotation than thermal electrons (Jones & O'Dell, 1977), and if the beam fluid is composed of electrons and positrons only, there is no Faraday rotation since the particles respond to circularly-polarized radiation in equal but opposite ways.

A final, major, complication to the use of the observed synchrotron radiation as an indicator of the underlying flow is the question of what relation the emission that we see has to the flow itself. Is the plasma that is *radiating* the same plasma that is *carrying the energy and momentum* in the beam, or even a constant fraction of it? In other words, are the large brightness variations seen in radio jets (such as the appearance of bright knots in the M 87 jet) produced by gross changes in the flow, or merely small changes in a trace population of relativistic electrons?

The answer to this question lies in the still unknown relationship between the properties of the bulk flow and the acceleration of relativistic particles within the beam. It is very likely that the electrons (and, perhaps, positrons) that are emitting synchrotron radiation are accelerated within the beam, and close to the regions in which the are observed, since their radiative lifetimes $\tau_{\rm e}$ are often shorter than the light travel time from the core of the source to the point at which they are detected, at least at high radio frequencies and in bright parts of jets. Thus the radio brightness is something close to a snapshot of the particle acceleration, and is, perhaps, showing us where in the flow the strong shocks lie, since these shocks are a likely site for accelerations (e.g., Blandford & Eichler 1987; Kirk 1994).

Similar considerations are important for the galactic jets. Much of the line emission that is seen arises from shocked gas, so that the material that is radiating may be only a thin layer around the material that carries most of the momentum.

2.2. The ambient medium

In extragalactic jets, the advent of a new generation of X-ray satellites has allowed us to get a good view of the medium around the jets. Thus, for example, near NGC 4261 the X-ray emission as seen by ROSAT is shown in Fig. 8. This emission consists of three components: an X-ray core (which is either non-thermal emission associated with the active nucleus of this galaxy, or thermal emission from a small-scale galactic atmosphere with high density), a small X-ray halo (Worrall & Birkinshaw 1994), and a group-gas halo with scale $\sim$ 25 kpc (Davis *et al.* 1995).

The X-ray data provide the temperatures of the extended gas. The density distribution of the gas near a radio source can be found either by fitting the image (usually to a symmetrical function; e.g., Worrall & Birkinshaw 1994) or by attempting a detailed deprojection. As a result, the distributions of pressure, density, and other gas properties in the ambient medium near the beam flow can be extracted reasonably well, although the data are rarely good enough for detailed temperature profiles to be measured. Table I presents the range of temperatures

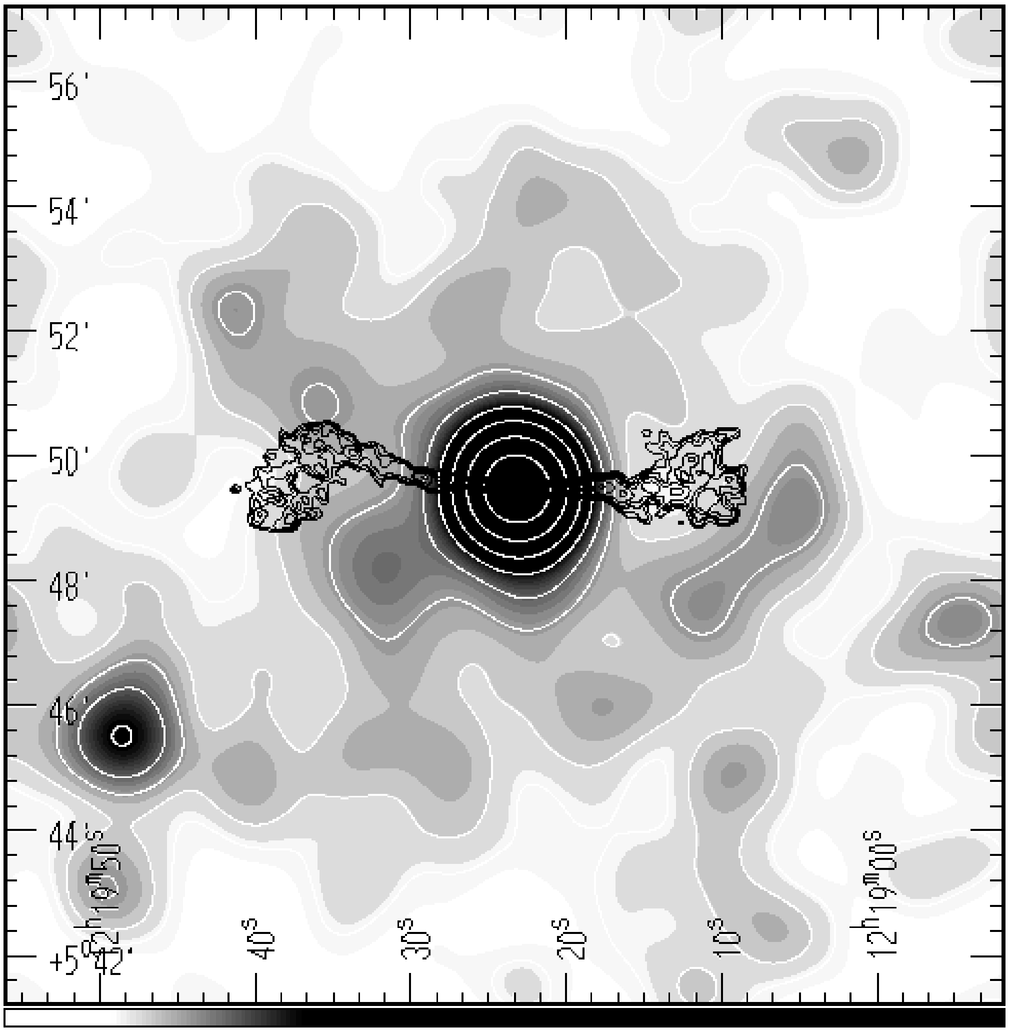

Fig. 8. A soft X-ray image of NGC 4261 made using the *ROSAT* PSPC. About half of the counts from the core of the galaxy lie in an unresolved component associated with the radio core of NGC 4261. The remainder lie in a halo with an angular scale $\sim$ 25 arcsec (4 kpc). In addition, there is clear evidence for larger-scale emission associated with the NGC 4261 group (Davis *et al.* 1995), which affects the dynamics of the outer parts of the radio source (3C 270).

and densities that are appropriate for large-scale jets, based on the range of gas properties of clusters and groups of galaxies given in the reviews of Forman & Jones (1982) or Sarazin (1986).

The parameters recorded in Table I should be extended to lower temperatures ($T_{\rm a} \sim 10^4$ K) and higher densities ($\rho_{\rm a} \sim 10^{-12}$ kg m^{-3}) if the jets in the broad–line and narrow–line emission regions in the active nuclei are to be discussed. However, here the medium is likely to be very clumpy, and strongly affected by the presence

TABLE I
The ambient medium

quantity	symbol	typical value		unit
		extragalactic	galactic	
sound speed	c_{Sa}	$300 - 1000$	$1 - 20$	$\mathrm{km\,s^{-1}}$
density	ρ_{a}	$10^{-25} - 10^{-22}$	$10^{-21} - 10^{-15}$	$\mathrm{kg\,m^{-3}}$
magnetic field	B_{a}	$0 - 1000$	$0 - 100$	nT
temperature	T_{a}	$10^6 - 10^8$	$10 - 10^4$	K
gas pressure	P_{a}	$10^{-15} - 10^{-10}$	$10^{-16} - 10^{-9}$	Pa
polytropic index	Γ_{a}	$\frac{5}{3}$	$\frac{7}{5} - \frac{5}{3}$	

of a high-power nuclear source that is emitting ionizing radiation. This makes it is difficult to make general statements about the environments of VLBI jets: each jet should be considered independently.

Similar remarks can be made about the environments of galactic jets. Here the properties of the gas can be found from the CO line emission from the molecular material in which the jet is embedded (or the HI line, if the jet is in a warmer environment; or the optical or X-ray emission in a few special cases, like SS 433). An example is L 1551, where the density in the cavity or the density in the surrounding molecular cloud can be obtained from the CO data. The inferred temperature of the ambient medium in which the jet lies is generally low (less than 30 K), but the densities may be high (for L 1551, $\sim 3 \times 10^9$ molecules $\mathrm{m^{-3}}$ before the cavity inflated, according to Snell & Schloerb 1985).

Just as for VLBI jets, the ambient medium in galactic jets is undoubtedly very clumpy. The widths of molecular lines from the surrounding molecular gas usually exceed the thermal line-widths predicted from the temperature (deduced from line strengths). This suggests that the surrounding gas is made up of denser cloudlets moving supersonically in a lower-density environment. Thus there is a significant probability that a beam in such an enviroment will hit a cloudlet, possibly with dramatic effects on the flow. Note also that galactic jets like SS 433, which is embedded in a supernova remnant, may be in a medium more like an extragalactic than a galactic jet.

In either the galactic or extragalactic cases the ambient medium is rarely uniform on the large scale. Thus, for example, the NGC 4261 jet has a size ~ 3 arcmin (35 kpc), comparable with the scale of the atmosphere in which it finds itself (Fig. 8). The external pressure therefore changes significantly on the scale of the jet. Thus the jets are never in a simple cylindrically-symmetrical flow, but are continually adjusting themselves to the properties of the medium that they flow through. This continuing adjustment may contribute to exciting the plasma that is flowing: perhaps helping it to generate the relativistic particles that cause the radio emission, or the collisionally-excited gas that we see from HH object complexes. It also suggests that a jet is never really in a steady state: beams are likely to change structure significantly on the timescales of sound crossings, and this may cause the jets that we see in our maps to be poor approximations to the mean flows that we want to understand.

In extragalactic jets the magnetic environments are now becoming better known through detailed rotation measure mapping. For example, the magneto–ionic halo around M 84 has been studied by Laing & Bridle (1987), who find magnetic fields $B_{\rm a} \sim 0.1$ nT which are ordered on scales of a few kpc, and Kim *et al.* (1986) have inferred large-scale fields of a similar strength in the Coma cluster. Larger fields are inferred from the enormous rotation measures seen in some sources (e.g., Cygnus A; Dreher *et al.* 1987). Even stronger external fields are necessary if jets are magnetically confined, and radial gradients of azimuthal field intensity are then expected: the upper limit to $B_{\rm a}$ in Table I reflects this possibility. The evidence for magnetic fields in the medium around galactic jets comes from measurements of Zeeman splittings (e.g., Goodman *et al.* 1989) or from arguments about compression of the Galactic magnetic field.

2.3. The beam fluid

The parameters of the beam fluid are much less certain. Let's start with galactic jets. Here the appearance of line emission allows good estimates of the gas density and temperature in the line-emitting part of the flow. For HH 34, for example, the electron density near in this gas is estimated to be about 10^9 electrons m^{-3} (Reipurth *et al.*, 1986), based on the strength of the [SII] emission lines. This emission is, however, from the shocked and radiating material that is likely to be associated only with the bow shocks of discrete units of the flow. The gas that is carrying most of the momentum in the beam may be much denser: indeed, the appearance of the HH 34 jet (Sec. 1.2.9) is more consistent with discrete lumpy ejection of material than a quasi-steady beam flow. Thus we will assume that galactic beams have a density that is similar to, or higher than, the density of the medium through which they move.

Since the material in the flow is radiating, the temperature in the unshocked gas is likely to be less than the temperature $\sim 10^4$ K to which radiation regulates an HII region. Furthermore, since this part of the flow does not seem to be radiating, the temperature is likely to be substantially lower. Hence outside the line-emitting regions of shocked material, the temperature should be $10 - 3000$ K, with sound speed within a factor ~ 10 of the sound speed of the ambient medium.

TABLE II
The beam

quantity	symbol	typical value extragalactic	typical value galactic	unit
core radius	R	$0.1 - 1000$	$10^{-5} - 10^{-2}$	pc
core speed	$v_{\rm b}$	$c_{\rm Sa} - 0.95c$	$c_{\rm Sa} - 0.95c$	
core sound speed	$c_{\rm Sb}$	$0.1 - 1000$	$0.1 - 10$	$c_{\rm Sa}$
core density	$\rho_{\rm b}$	$10^{-6} - 10^{2}$	$0.1 - 10^{3}$	$\rho_{\rm a}$
core magnetic field	$B_{\rm b}$	$0 - 1000$	$0 - 100$	nT
core fluid polytropic index	$\Gamma_{\rm b}$	$\frac{4}{3} - \frac{5}{3}$	$\frac{5}{3}$	
sheared region width	δ	$0 - 2$	$0 - 2$	
sheared fluid polytropic index	$\Gamma_{\rm s}$	$\frac{4}{3} - \frac{5}{3}$	$\frac{5}{3}$	

The speeds of galactic flows can be seen directly, from the proper motions of the knots, as well as estimated from the velocities of the line-emitting gas relative to the velocity of the originating object: indeed, by measuring both speeds, the full 3-dimensional velocity of the knots can be measured, and the orientation of the jet to the line of sight can be found. The typical speeds of prominent flows in star-forming regions (such as the HH 34 jet) are a few hundred $\rm km\,s^{-1}$, but it is likely that many weaker flows also exist.

The magnetic fields in these jets are essentially unknown, so we will assume values similar to those in the external medium, and rely on the results of detailed calculations (yet to be done: an excellent thesis project) to investigate the possible consequences of stronger fields.

Of course, the discussions above relate only to the types of jet seen in star-forming regions. The other class of galactic jets, such as SS 433, is in some ways similar, but may contain much stronger magnetic fields (which, together with their relativistic particles, are responsible for the radio emission), and are certainly faster flows! A summary of the results for galactic beams is given in Table II.

In extragalactic jets there is rarely any direct indication of the flow velocity. Where there is structural change, for example in VLBI jets, the apparent velocities are often much larger than the speed of light. This is explained as a consequence of relativistic motion in the source (Fig. 9): if the jet contains a knot that is moving with speed $v_{\rm knot}$, and the jet lies at an angle θ to the line of sight, then the observer

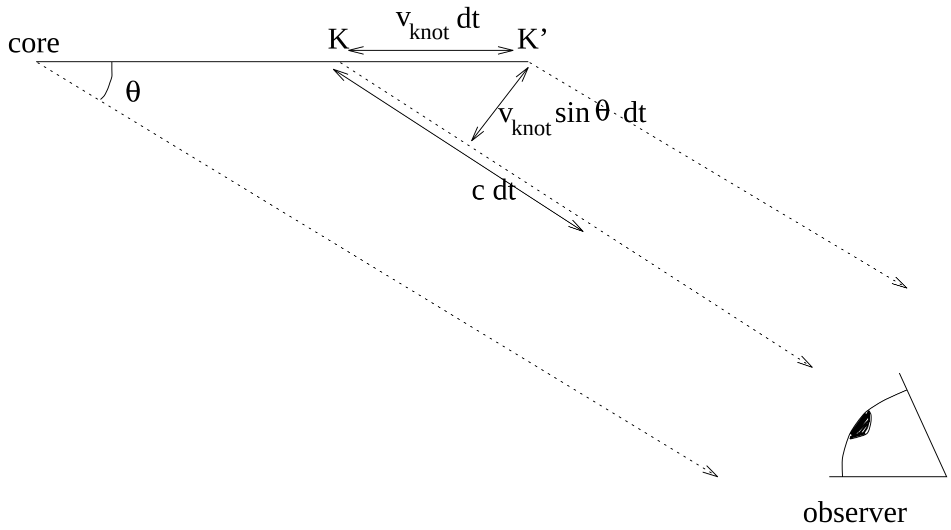

Fig. 9. The geometry of superluminal motion occuring as a result of relativistic motion near the line of sight. In the interval dt, the knot K moves to K$'$, a projected distance $v_{\rm knot}\sin\theta\,dt$ away, from the observer's point of view. In the same interval, light pulses from K and K$'$ are separated by $dt\,(c - v_{\rm knot}\cos\theta)$, so that the apparent time taken for the motion from K to K$'$, as seen by the observer, is $dt\,(c - v_{\rm knot}\cos\theta)/c$, and the apparent transverse velocity of the knot is therefore given by (11).

will see a motion across the line of sight with apparent velocity

$$v_{\rm app} = v_{\rm knot}\sin\theta\left(1 \pm \frac{v_{\rm knot}}{c}\cos\theta\right)^{-1} \tag{11}$$

where the positive sign indicates an approaching knot. Then if $v_{\rm knot} > c/\sqrt{2}$, $v_{\rm app}$ can exceed c for some orientations of the jet to the line of sight. For VLBI jets, where speeds $> 10c$ have been observed, it is clear that $v_{\rm knot}$ must be close to c. Interestingly, (11) has been used for GRO 1655-40 to obtain limits on both the velocity $v_{\rm knot}$ and on the angle θ, using the angular velocity difference on the two sides of the core (Hjellming & Rupen, 1995).

A major issue in the use of (11) is whether the observed motions in VLBI jets are indicators of the true motion of the bulk flow, or of a moving pattern of material within the flow. A simple example of a situation where the pattern speed can exceed the flow speed is shown in Fig. 10. If two oblique waves within the beam are converging from the edges of the beam towards the center (perhaps as the result of an expansion of the beam), and we identify the region of brightest radio emission with the point at which these fronts cross (which is where the strongest particle acceleration is likely), then the speed with which the crossing point advances up the flow is $v_{\rm shock}/\sin\alpha$. If we assume that the beam is heated

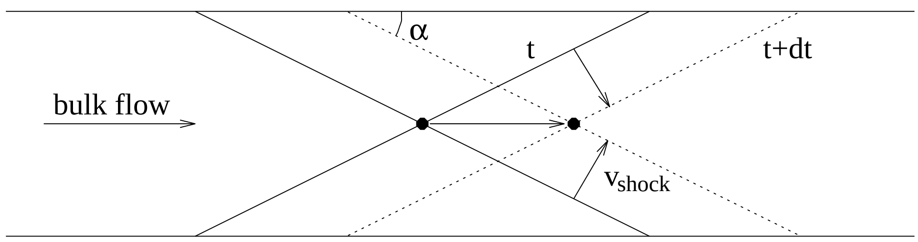

Fig. 10. A simple example of a pattern speed that is different from the flow speed. Suppose that a radio knot is identified with the crossing point of two shocks which converge from the edge of the beam. Then in time dt, the shocks move distance $v_{\rm shock}\, dt$ while the crossing point moves $v_{\rm shock}\, dt/\sin\alpha$. The pattern speed of the crossing point is therefore $v_{\rm shock}/\sin\alpha$, which may exceed the speed of the bulk flow.

so that the internal sound speed is comparable with the flow speed, then it is clear that the crossing point will advance faster than the flow speed even for large angles α, and may be much faster for small α.

For the larger-scale jets only indirect arguments exist for the beam velocities, and the results quoted in the literature are model-dependent and unreliable. In many cases it is not clear whether the flows are relativistic or non-relativistic. Some velocities are derived on a ballistic model for the jets, in which the flows are undecelerated (and, for 3C 449, for example, the speeds that are fitted must be a few times the escape speed from the host galaxy if interesting bends are to be formed; Blandford & Icke 1978). Other speeds are often based on a balance between the radiated energy from the radio source and the energy carried down the beam, after using a density estimate derived from the Faraday depolarization. Unfortunately, the measurement of Faraday depolarization is fraught with difficulties (see the review by Leahy 1991), and the resulting velocities are not reliable. Perhaps the best indications about beam speed are obtained by looking at simulations: to produce flows that *look* like FR 2 jets, light, supersonic flows are needed. For FR 1 jets, slower speeds may suffice. However, it is clear that the speeds are *at least* sufficient for the flow to escape from the host galaxy, and are hence a few times the sound speed. The entry in Table II is suitably cautious.

As mentioned above, there is little reliable information on the flow density either. If the Faraday depolarization is known, then some magnetic field can be guessed (perhaps from the minimum energy argument, see later), and the density estimated, but this always implies a model for the locations of the relativistic particles, fields, and energy-carrying material within the flow and we know (e.g., from M 87) that the distribution of radio emission can be complicated. Furthermore, we do not know whether the jet material is "conventional" astrophysical material, an electron/positron mixture, or some combination. It is only when the positive and negatively charged particles have different masses that the density can be obtained through Faraday depolarization. The best indication of density, then, is presumably again the simulation results, and I shall assume that the beams of extragalactic jets are generally very light.

The radii of extragalactic radio jets, R, vary from less than 1 parsec in VLBI jets to more than 1 kpc in low–power radio sources, or in the outer parts of high-power sources. In general, though, R is less than the scale on which we expect significant pressure structures in the external medium (except for shocks or dense blobs, which are most likely in the nuclear environment of VLBI jets).

Presumably the flowing beam is close to sideways dynamical equilibrium: that is, it is in contact with the surrounding gas and its internal pressure (from magnetic field, thermal gas, and relativistic particles) is close to being in balance with the external pressure. For fast flows this is not the pressure of the ambient medium, but rather the significant over-pressure of the cocoon (Loken *et al.*, 1992).

It is conventional to estimate the internal pressure of a beam using the minimum energy argument to estimate the magnetic field and the relativistic particle energy density, and then assuming some field geometry. The minimum energy argument consists of minimising the total energy density in some section of the radio source, while keeping the observed brightness (given by 7) constant. The result that is obtained is

$$B \propto ((1+k)\ L_\nu)^{2/7} \tag{12}$$

Burbidge (1956), where k is the ratio of the energy densities in non-radiating particles and radiating electrons (and positrons), and L_ν is the synchrotron luminosity at some frequency. However, the existence of the "fiddle factor" k, which is essentially unknown, and the suspicion that the source may not be "efficient" in the sense of producing the maximum radio emission for a given relativistic electron population prevents the estimated pressures from being more than crude lower limits.

If we apply this argument, with $k = 0$ which implies that the non-relativistic component of the flow does not contribute to the pressure, then weak radio sources such as 3C 449 and NGC 6251 exhibit minimum pressures of 10^{-14} to 10^{-11} Pa, so that the thermal pressure of the ambient medium (up to 10^{-10} Pa; Table I) can confine the jets (Fig. 11; but see Birkinshaw & Worrall 1991). For the most powerful jets in quasars and high–power radio galaxies, on the other hand, the assumption that the beams are confined implies that the external magnetic field or the jet cocoon is making a significant contribution to the pressure, since the ambient pressure is clearly insufficient to confine the beam.

The mixture of relativistic gas and thermal particles in the beam is generally treated as a single fluid, with no explicit account being taken of the transfer of energy between the constituents of the fluid. It is generally assumed that the beam fluid is a neutral mixture of electrons and protons, and this assumption will

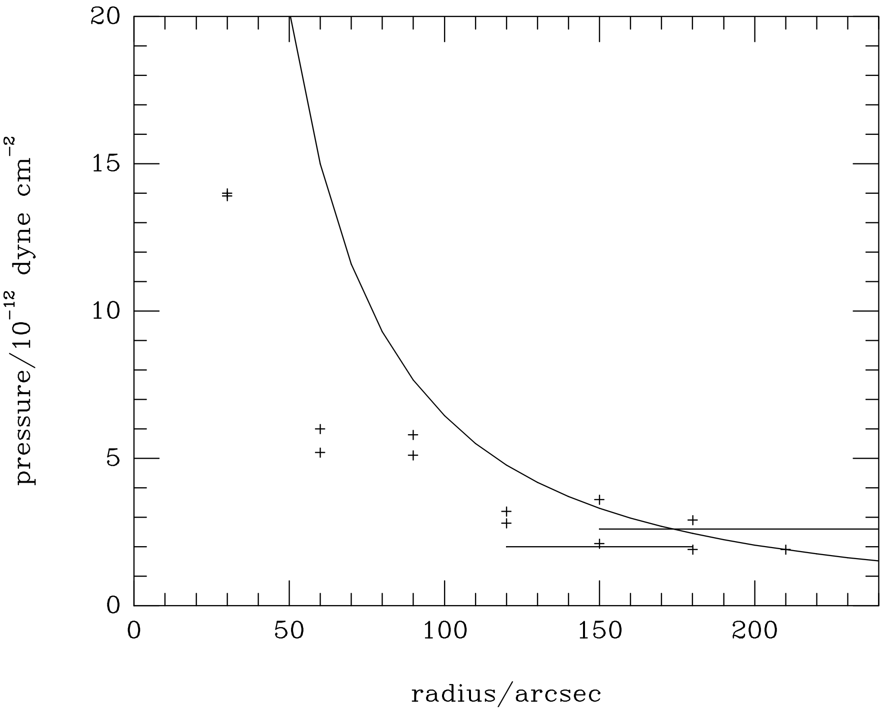

Fig. 11. Pressures in and near the radio jets of NGC 4261, assuming that the source lies in the plane of the sky. Points indicate total pressures in the E and W jets, and the horizontal lines mark estimates of the total pressure in the radio lobes (assuming that only electrons and magnetic fields contribute). The external pressure, shown by the curve, exceeds the internal minimum pressure over the entire radio jet and is about equal to the lobe minimum pressure.

be made here, but the beams may consist of an electron–positron fluid (see, for example, Burns & Lovelace 1982).

Just as we are uncertain about the velocity, density, and pressure of a beam, we are uncertain about its internal structure. Until we can do real plasma diagnostics on jets there is little we can do about this: my approach here is to treat the beam core as being a uniform flow, and the ambient medium as a second uniform flow, and then put all the messy assumptions about structure into a "shear layer" dividing the two. In the notation of Table II (and Figure 12), this shear layer is given a scale δ, defined as

$$\delta = 2\frac{R_{\rm sa} - R_{\rm bs}}{R_{\rm sa} + R_{\rm bs}} \tag{13}$$

which varies from zero (no shear layer) to two (no beam core).

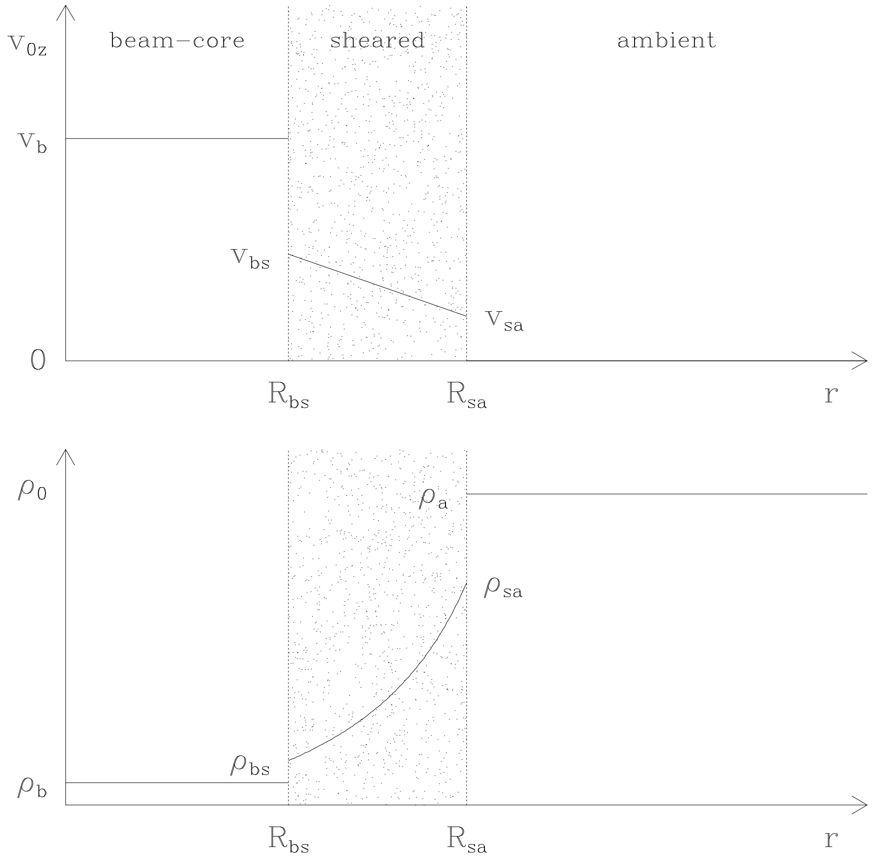

Fig. 12. A schematic diagram of a beam structure including a uniform beam core (of radius $R_{\rm bs}$, density $\rho_{\rm b}$, and velocity $v_{\rm b}$) and a uniform ambient medium (of radius $R_{\rm sa}$, density $\rho_{\rm a}$, and at rest) separated by a shear layer of dimensionless thickness δ (13) where the density varies from $\rho_{\rm bs}$ to $\rho_{\rm sa}$ as the velocity drops from $v_{\rm bs}$ to $v_{\rm sa}$. The radius of the beam is identified with the mid-point of the shear layer, $R = (R_{\rm sa} + R_{\rm bs})/2$.

2.4. Dimensionless numbers

Let's use the parameters in the Tables to derive some facts about the flows that we are discussing. First, let's consider the role of the magnetic field. A parameter that captures the relative importance of particle pressure and magnetic fields to the dynamics is

$$\beta_{\rm P} = \frac{P}{u_{\rm B}} \tag{14}$$

where P is the fluid pressure and $u_{\rm B}$ is the magnetic field energy density. For the ambient medium, far from the beam, it is likely that $\beta_{\rm P}$ is very large. For a typical cluster of galaxies, $\beta_{\rm P} \gtrsim 10^3$, and the magnetic field is not dynamically important. If the larger field strengths in Table I or II are taken with the smaller fluid pressures, however, small values of $\beta_{\rm P}$ may result, and magnetic fields could dominate the flow. This can also be said in terms of the Alfvén speed,

$$c_{\rm A} = \frac{B}{(\mu_0\,\rho)^{1/2}}. \tag{15}$$

Magnetic fields become important when the Alfvén speed approaches the sound speed in the gas.

In discussing the flow so far, we have been referring to the flow velocity as if it were a well-defined quantity. However, if the beam flow is turbulent, then we have been discussing only the *mean flow velocity* and other mean flow parameters. The Reynolds number describes whether an astrophysical beam can support turbulence: for magnetically–active plasmas we use the usual fluid Reynolds number

$$Re = \frac{\rho\,v\,l}{\eta}, \tag{16}$$

and the magnetic Reynolds number

$$Re_{\rm m} = v\,l\,\sigma\,\mu_0, \tag{17}$$

where v is the velocity scale and l is the length scale of the flow ($v \approx v_{\rm b}$ and $l \approx R$). ρ, η, and σ are the density, viscosity, and electric conductivity of the fluid, respectively, and μ_0 is the permeability of free space. Using representative values for the temperature, magnetic field, density, velocity, and radius of a jet (from Table II) and the expressions for σ and η given by Spitzer (1962), these Reynolds numbers may be calculated to be

$$Re \sim 4 \times 10^{28} \tag{18}$$

and

$$Re_{\rm m} \sim 10^{28} \tag{19}$$

unless the velocity and velocity gradient in the flow are accurately parallel to the magnetic field.

The large value of $Re_{\rm m}$ indicates that magnetic field diffusion is much less important than the advection of the field by the flow (but note that this may not be true in thin *current sheets*, where large energy releases can take place). The large value of Re implies that turbulent motions are almost undamped, and astrophysical beams should be highly turbulent. Although much work on turbulent flows has been done under particular assumptions about the physics of the processes involved (Bicknell, 1984; Henriksen, 1987), the lack of definite knowledge about turbulence, particularly supersonic turbulence, makes it difficult to evaluate these results.

Perhaps the most important dimensionless number for describing these flows is their Mach number. Using the values in Tables I and II, we can calculate an external Mach number

$$\mathcal{M}_{\mathrm{a}} = \frac{v_{\mathrm{b}}}{c_{\mathrm{Sa}}} = \begin{cases} 1 - 10^5 & \text{extragalactic} \\ 1 - 10^8 & \text{galactic} \end{cases} \tag{20}$$

where the extreme values for galactic jets arise in cases like GRO 1655-40. Thus in most cases we are dealing with supersonic or transsonic flows, and some hypersonic flows are also likely.

A parameter η is also in common use. η is the density ratio of the beam and the ambient medium: $\eta > 1$ is a dense flow, $\eta < 1$ is a light flow. The parameter range specified in Table II allows for either light or dense beams in extragalactic and galactic flows.

Finally, we should examine the continuity of the flows. Many jets, particularly the most powerful jets, are one–sided. This has been taken as evidence for Doppler preference, but also as evidence that the ejection is intrinsically one-sided (Burns, 1984), when the directions of jet ejection must vary on timescales much less than the flow time from the core to the lobes (Rudnick & Edgar, 1984). The ages of jets are easy to determine where jet motions are seen (in the galactic cases): star formation only produces jets over a small fraction of the time that the entire process takes. For GRO 1655-40, we believe that the jet started at about the time that the source was detected (Sec. 1.2.8). For the extragalactic sources, the ages are determined from spectral features which indicate which electrons have radiated all their energy: the age of the source is then related to the corresponding τ_{e} (Sec 2.1). However, no well-determined jet spectral feature exists that can be used to test the duty cycle or turn-on time of an extragalactic jet.

2.5. Equations of motion of beams

In accordance with the arguments given above, we model the beam fluid flows as an inviscid, electrically–conducting (but not heat–conducting), compressible, relativistic gas moving in the absence of any gravitational field. The equations describing this motion are the equation of conservation of energy and momentum

$$T^{\mu\nu}{}_{,\nu} = 0. \tag{21}$$

The energy–momentum tensor $T^{\mu\nu}$ contains the energy and momentum of the fluid and the electromagnetic field $T^{\mu\nu} = T^{\mu\nu}_{\mathrm{fluid}} + T^{\mu\nu}_{\mathrm{EM}}$, where

$$T^{\mu\nu}_{\mathrm{fluid}} = (\rho + \frac{P}{c^2})\, u^\mu u^\nu + P\, \eta^{\mu\nu} \tag{22}$$

$$T^{\mu\nu}_{\mathrm{EM}} = \frac{1}{\mu_0} \left(F^{\mu\alpha}\, F^{\nu}{}_{\alpha} - \frac{1}{4} F^{\alpha\beta}\, F_{\alpha\beta}\, \eta^{\mu\nu} \right). \tag{23}$$

The density of the fluid, ρ, includes both the rest–mass and the mass equivalent of the energy density of the fluid, P is the pressure of the fluid, and u^μ is the usual velocity four–vector. Greek indices are assumed to run from 0 to 3, and $\eta^{\mu\nu}$, the Minkowski metric tensor, is defined according to a spacelike convention. $F^{\mu\nu}$ is the electromagnetic field tensor. μ_0 is the permeability of free space, and the relative permittivity and permeability of the fluid, ϵ and μ, are assumed to be unity.

In addition to the equations of motion, an equation is needed to describe the presence of a gradient in the entropy due to the density and velocity shears and the generation of entropy by Joule heating. This entropy equation is

$$(n\,s\,u^\mu)_{,\mu} = -\frac{1}{T}\,u_\mu\,F^{\mu\nu}\,J_\nu, \tag{24}$$

where n is the baryon number density, s is the entropy per baryon in the fluid, T is the temperature of the fluid and J^μ is the charge–current four–vector.

The electromagnetic field tensor $F^{\mu\nu}$ obeys the Maxwell equations

$$F_{\alpha\beta,\gamma} + F_{\beta\gamma,\alpha} + F_{\gamma\alpha,\beta} \;=\; 0 \tag{25}$$

$$F^{\alpha\beta}{}_{,\beta} \;=\; \mu_0\,J^\alpha \tag{26}$$

which imply the equation of conservation of electric charge, $J^\mu{}_{,\mu} = 0$.

We also require a constitutive equation describing the relation between the charge current and the fields (the conduction equation),

$$J^\mu + \frac{u^\mu u_\nu}{c^2}\,J^\nu = \sigma\,F^{\mu\nu}\,u_\nu \tag{27}$$

where σ is the electrical conductivity (written as a scalar here, for simplicity).

Finally, we have equations describing the interrelation of the thermodynamic parameters n, ρ, P, s, and T. These equations are the equation of baryon conservation

$$(n\,u^\mu)_{,\mu} = 0, \tag{28}$$

two equations of state

$$P \;=\; P(n,s) \tag{29}$$

$$T \;=\; T(n,s), \tag{30}$$

and the first law of thermodynamics

$$d\rho = (\rho + \frac{P}{c^2})\,\frac{dn}{n} + \frac{n\,T}{c^2}\,ds \tag{31}$$

(Landau & Lifshitz 1959; Misner *et al.* 1973; Königl 1980).

These equations can be written in terms of variables $\mathbf{E}$, $\mathbf{B}$, $\mathbf{j}$, $\rho_{\rm c}$, ρ, P, $\mathbf{v}$, n, s and T, as

$$\begin{aligned}
\frac{\partial}{\partial t}\left(\gamma^2(\rho+\frac{P}{c^2})-\frac{P}{c^2}\right)+\nabla.\left(\gamma^2(\rho+\frac{P}{c^2})\mathbf{v}\right) &= \frac{\mathbf{E}.\mathbf{j}}{c^2} && (32)\\
\gamma^2(\rho+\frac{P}{c^2})\left(\frac{\partial\mathbf{v}}{\partial t}+(\mathbf{v}.\nabla)\mathbf{v}\right)+\nabla P+\frac{\mathbf{v}}{c^2}\frac{\partial P}{\partial t} &= \rho_{\rm c}\mathbf{E}+\mathbf{j}\times\mathbf{B}-\frac{\mathbf{v}}{c^2}(\mathbf{E}.\mathbf{j}) && (33)\\
nT\left(\frac{\partial s}{\partial t}+\mathbf{v}.\nabla s\right) &= (\mathbf{E}.\mathbf{j}-\mathbf{v}.\mathbf{j}\times\mathbf{B}-\rho_{\rm c}\mathbf{v}.\mathbf{E}) && (34)\\
\frac{\partial(\gamma n)}{\partial t}+\nabla.(\gamma n\mathbf{v}) &= 0 && (35)\\
\nabla.\mathbf{E} &= \frac{\rho_{\rm c}}{\epsilon_0} && (36)\\
\nabla.\mathbf{B} &= 0 && (37)\\
\nabla\times\mathbf{E} &= -\frac{\partial\mathbf{B}}{\partial t} && (38)\\
\nabla\times\mathbf{B} &= \mu_0\mathbf{j}+\frac{1}{c^2}\frac{\partial\mathbf{E}}{\partial t} && (39)\\
\gamma(\mathbf{v}.\mathbf{j}-\rho_{\rm c}\mathbf{v}.\mathbf{v}) &= \sigma\,\mathbf{v}.\mathbf{E} && (40)\\
\mathbf{j}+\frac{\gamma^2}{c^2}\mathbf{v}(\mathbf{v}.\mathbf{j}-\rho_{\rm c}c^2) &= \gamma\,\sigma(\mathbf{E}+\mathbf{v}\times\mathbf{B}). && (41)
\end{aligned}$$

where

$$\gamma = \left(1-\frac{\mathbf{v}.\mathbf{v}}{c^2}\right)^{-1/2}. \qquad (42)$$

These equations may be simplified for the highly–conducting plasmas of astrophysical beams, since the large value of the magnetic Reynolds number $Re_{\rm m}$ causes $F^{\mu\nu}u_\nu \approx 0$, or equivalently

$$\mathbf{E} = -\mathbf{v}\times\mathbf{B} \qquad (43)$$

to an accuracy $O(Re_{\rm m}^{-1})$, or about one part in 10^{28}.

The assumption that the astrophysical plasma behaves as a continuum, which is essential if these equations are to apply, is excellent in the cases in which we are interested: the Debye length, $\lambda_{\rm D} = (\epsilon_0 k_{\rm B}T/ne^2)^{1/2}$, and the particle gyroradii are always smaller than the jet scales. Furthermore, we expect the fields and flows to change slowly compared with the time on which the plasma re–adjusts to charge neutrality. That is, the frequencies of interest are much lower than the plasma frequency, the ion gyrofrequency, and so on.

Formally, (29 – 43) describe the beam and the ambient medium together by a single set of velocity, density, pressure, and magnetic field functions. However, the problem is simplified by defining boundaries between regions of the flow which are described by different functions. One convenient choice, shown in Fig. 12, is to refer to the flow as three distinct regions (the beam core, the sheared flow, and the ambient medium), where only one of these regions (the sheared flow) contains gradients in the velocity or density. The functions describing the flow are then matched at the interfaces between these artificial domains.

2.5.1. *The relativistic, non-magnetic, equations of motion*
A simpler case of (29 – 43), which has been subjected to theoretical analysis, is that of relativistic, non–magnetic, flows, for which the equations reduce to the set

$$\frac{\partial}{\partial t}\left(\gamma^2(\rho+\frac{P}{c^2})-\frac{P}{c^2}\right)+\nabla.\left(\gamma^2(\rho+\frac{P}{c^2})\,\mathbf{v}\right) = 0 \tag{44}$$

$$\gamma^2(\rho+\frac{P}{c^2})\left(\frac{\partial\mathbf{v}}{\partial t}+(\mathbf{v}.\nabla)\mathbf{v}\right)+\frac{\mathbf{v}}{c^2}\frac{\partial P}{\partial t}+\nabla P = 0 \tag{45}$$

$$\frac{\partial s}{\partial t}+\mathbf{v}.\nabla s = 0 \tag{46}$$

$$s = s(P,\rho) \tag{47}$$

which may be recognised as the usual equations of relativistic fluid flow. Codes that solve these equations in full generality are rare.

2.5.2. *The non-relativistic, magnetic flow*
The basic equations of fluid motion for an ideal, compressible, magnetic fluid in non–relativistic motion ($v \ll c$) can be derived from the general equations of motion as

$$\frac{\partial\rho}{\partial t}+\nabla.(\rho\mathbf{v}) = 0 \tag{48}$$

$$\rho\left(\frac{\partial\mathbf{v}}{\partial t}+(\mathbf{v}.\nabla)\mathbf{v}\right) = -\nabla P+\frac{1}{\mu_0}(\nabla\times\mathbf{B})\times\mathbf{B} \tag{49}$$

$$\frac{\partial s}{\partial t}+\mathbf{v}.\nabla s = 0 \tag{50}$$

$$s = s(P,\rho) \tag{51}$$

$$\nabla.\mathbf{B} = 0 \tag{52}$$

$$\frac{\partial\mathbf{B}}{\partial t} = \nabla\times(\mathbf{v}\times\mathbf{B}). \tag{53}$$

These equations represent a considerable simplification, but the presence of the magnetic field causes additional difficulties over the non–magnetic case, although all relativistic effects have been ignored.

3. Kelvin-Helmholtz instabilities

If we are to accept the beam model (Section 2), so that jets are interpreted in terms of a directed flow from a compact object into a diffuse medium, then at least some beams must be sufficiently stable that they can preserve their identity and ability to transport energy over a distance of many jet radii (see the examples in Section 1).

This Section is concerned with the stability of beam flows. The subject is rather technical, but leads to some interesting conclusions, and some of the methods can be used in other stability problems. Generally, work on beam stability has used (analytical) linear instability theory (*e.g.*, Chandrasekhar 1961; Drazin & Reid 1981). This methodology has been fairly successful at describing the stability of laboratory free shear flows (see the review of Ho & Huerre 1984): the extension to astrophysical flows needs to take account of the compressibility of the beam fluid, the presence of magnetic fields, and the possibility of energy loss through radiation.

3.1. Linear instability theory

Plasma instabilities can be divided into the categories of *microinstabilities*, where the details of the distribution functions of particle species in the plasma are essential, and *macroinstabilities*, where only the bulk equations of motion of the fluid are necessary to describe the instability. Only macroinstabilities operate on large scales, such as the radius of a beam, and directly affect the gross pattern of flow. The Kelvin–Helmholtz instability is a classic example of a macroinstability: its natural length scale is a beam radius, and its time scale is a beam sound crossing time. By contrast, the two-stream instability, a well-known microscopic instability, operates at the characteristic timescale of plasma oscillations.

Kelvin–Helmholtz instabilities arise when two fluids are in relative motion on either side of some common boundary. Their origin may be traced to the Bernouilli equation—if a ripple develops at the interface, then fluid flowing faster to pass over that ripple exerts less pressure, and the ripple tends to grow. Kelvin–Helmholtz modes grow into striking wave structures (*e.g.*, Roberts *et al.* 1982).

The large-scale instability of a specific beam can be examined using numerical methods (e.g., Hardee & Clarke 1992), and numerical techniques are essential to check whether an instability grows to disrupt the beam or is stopped by some dissipative mechanism. However, analytical methods give an indication of stability for a variety of beam parameters without needing to run detailed numerical models for each case, and can check a wide range of linear scales in a problem, including scales which might be beyond the resolution limit of a particular numerical calculation.

What do we mean by "instability"? Generally, a fluid system is said to be unstable if small perturbations of that system grow. Note that large perturbations may be unstable even if small perturbations of all kinds are stable, and the flow that results from the growth of small perturbations may be stable (we say that the growth of the small perturbations *saturates*). An instability may disrupt the flow entirely, or it may cause the flow to readjust into a new configuration, which may itself be stable or unstable.

The simplest type of linear instability analysis revolves around a *dispersion relation*

$$\mathcal{D}(\omega, \mathbf{k}) = 0 \tag{54}$$

where perturbations $V^{(1)}$ of fluid variable V are assumed to be of the form

$$V^{(1)} \approx e^{i(\mathbf{k}.\mathbf{r}-\omega t)}. \tag{55}$$

The stability of the flow is then inferred from the behaviour of the *complex* angular frequency (ω) or wavevector ($\mathbf{k}$) roots of (54). If ω is assumed to be real, then roots of (54) with a negative imaginary part of $\mathbf{k}$ correspond to (spatially) growing perturbations in some direction: this is *spatial instability.* Alternatively, $\mathbf{k}$ can be assumed to be real, when the presence of roots with a positive imaginary part of ω indicates *temporal instability.*

The spatial instability formalism seems appropriate for beam flows, where an unstable disturbance propagates downstream as it grows. Nevertheless, the applicability of spatial instability theory is a subtle issue. A spatially growing mode will, according to (55), have infinite amplitude far downstream of its point of origin, and this contradicts the usual boundary condition for unstable modes—that they should tend to zero at a large distance from their source. The contradiction is usually more apparent than real, because it is usually the case that the growth of the mode to a large amplitude at far downstream points occurs *after* it grows to large amplitude at some fixed location—i.e., the relative amplitude does decline as a function of distance from the source. Clemmow & Dougherty (1969) find that spatial and temporal descriptions of instability are equivalent in cases where the real ω axis can be smoothly transformed to the real k, and that this is the case in free shear flows like the beams in which we are interested.

The survival of astrophysical beams is largely determined by their response to the Kelvin–Helmholtz instability. The study of Kelvin–Helmholtz instabilities on radio jets was introduced by Turland & Scheuer (1976) and Blandford & Pringle (1976) to test the feasibility of the transport of energy to the outer parts of radio galaxies. In this context, the presence of instabilities is *undesirable*, because they inhibit the effective transport of energy. The possibility that instabilities on the jet of M 87 might cause the optical knots was discussed by Stewart (1971), and Hardee (1979) has emphasized the possibility that instabilities on radio jets might cause knots and bends which resemble observed jet structures. Instabilities have also been invoked as causes of the distorted lobes of radio sources (Blake, 1972) and the shapes of comet tails by (Ershkovich, 1980; Kochhar & Trehan, 1988), and as a source of energy that might cause *in situ* particle acceleration (Ferrari *et al.* 1979). In this context, the presence of instabilities is seen as *desirable.* Overall the study of beam stability aims

– to discover whether there are beam structures capable of transporting energy to radio lobes without being wholly disrupted; and

– to determine whether particle acceleration and structural distortions may arise through the operation of instabilities which do not disrupt beams.

A dispersion relation such as (54) is derived under the assumption that the perturbations are sufficiently small that the fluid/plasma equations are linear in the perturbation variables. This assumption ceases to be true when the perturbations grow to observable sizes, so that linear analyses can predict *at most* the scales and types of structure that *might* develop. At this point different (often numerical) methods must be used to decide whether the instability develops to cause a detectable change in the flow. If the flow develops shocks, then they provide an opportunity for particle acceleration, and can cause abrupt changes in the direction or the physical properties of the beams. Alternatively, the instability might lead to the formation of *solitons*, non–linear disturbances that propagate with no (first order) change of shape, and which retain their identity in collisions with other solitons. The vortex rings developed around jets observed in the laboratory may be disturbances of this type. Lerche & Wiita (1980), Fiedler (1986), and Roberts (1987) have investigated this possibility. Instabilities seem likely to cause the beam flow to become make the transition to turbulence, with the turbulent energy cascade causing particle acceleration (Ferrari *et al.* 1979) and heating the beam material.

3.2. A model of the steady-state flow

The discussion of beam stability begins with a description of its steady–state structure. Analytical studies are restricted to flows which are slowly–varying and near pressure equilibrium, so that the steady–state flow is relatively simple. The flow may be laminar or turbulent, but the lack of a convincing theoretical description of turbulence leads us to consider the development of instabilities on a laminar jet. Jets of circular section are of greatest interest for astrophysicists, and a plausible model structure is sketched in Fig. 12, where the velocity profile $v_z^{(0)}(r)$ and the density profile $\rho^{(0)}(r)$ of the unperturbed flow are defined for a model flow with a constant radius.

In Fig. 12, I have divided the model beam into three segments: a beam core (subscript b), the ambient medium (subscript a), and a sheared region between them (subscript s). The ambient medium will be assumed to be uniform, with no density, temperature, or magnetic field gradients that might cause the steady–state flow to be non–cylindrical. Where this is not the case, for example if the density of the ambient medium is decreasing in the direction of the flow, then it this structure must be explicitly modeled. Rapid variations in the properties of the ambient medium cause the instability problem to become intractable: for long–wavelength instability modes the nonuniformity of the ambient gas will limit the applicability of the model.

Analytical instability studies are restricted to flows near dynamical equilibrium, where the total internal pressure in the beam balances the external pressure of the ambient medium. If the jets are *free*, and not in effective contact with the ambient medium, then the instability analyses described here are inapplicable. It is also necessary that we take the unperturbed flows as being steady on the timescales of interest.

If we adopt the relativistic equations of motion developed in Sections 2.5.1 and 2.5.2, then a simple solution in cylindrical coordinates, (r, θ, z), which describes an unperturbed beam with significant structure is a steady, non–rotating, cylindrical beam flow with

$$\rho = \rho^{(0)}(r) \tag{56}$$

$$\mathbf{v} = (0, 0, v_{\mathrm{z}}^{(0)}(r)) \tag{57}$$

$$\mathbf{B} = (0, B_{\theta}^{(0)}(r), B_{\mathrm{z}}^{(0)}(r)) \tag{58}$$

where $\rho^{(0)}(r)$, $v_{\mathrm{z}}^{(0)}(r)$, $B_{\theta}^{(0)}(r)$ and $B_{\mathrm{z}}^{(0)}(r)$ are arbitrary functions of the distance from the beam axis, r. The pressure, $P = P^{(0)}(r)$, must then obey the equation of transverse force equilibrium

$$\frac{dP^{(0)}}{dr} = \frac{1}{\mu_0}\left(B_{\theta}^{(0)2}\frac{v_{\mathrm{z}}^{(0)}}{c^2}\frac{dv_{\mathrm{z}}^{(0)}}{dr} - \frac{1}{\gamma^{(0)2}}\frac{B_{\theta}^{(0)}}{r}\frac{d}{dr}(rB_{\theta}^{(0)}) - B_{\mathrm{z}}^{(0)}\frac{dB_{\mathrm{z}}^{(0)}}{dr}\right) \tag{59}$$

where $\gamma^{(0)}(r)$ is the local Lorentz factor,

$$\gamma^{(0)}(r) = \left(1 - \frac{v_{\mathrm{z}}^{(0)2}}{c^2}\right)^{-1/2}. \tag{60}$$

(56 – 60) formally describe the beam, ambient medium, and shear layer by a single set of model functions. It is generally much more convenient to define boundaries between regions of the flow, and then use different model functions in each region, as has been done in Fig. 12. The functions describing the flow are then matched at the interfaces between these artificial domains.

3.3. Some dispersion relations

The steady–state solutions (56 – 60) are written with suffix $^{(0)}$, as in the unperturbed pressure, $P^{(0)}$. To investigate the stability of this solution, the physical variables are expanded as sums of the unperturbed $^{(0)}$ parts and small $^{(1)}$ perturbations (for example, $P = P^{(0)} + P^{(1)}$). These forms for the variables are then substituted into the equations of motion (Sections 2.5.1 and 2.5.2), and the equations are linearized (expanded to first order in the perturbed quantities) by requiring that the perturbed flow variables are much smaller than the unperturbed variables (for example, $v_{\rm r}^{(1)} \ll v_{\rm z}^{(0)}$). The resulting equations are homogeneous in the perturbed quantities, but are too complicated for most purposes. Analyses of the stability of beam flows are based on simplifying assumptions about the functions $\rho^{(0)}$, $v_{\rm z}^{(0)}$, $B_\theta^{(0)}$, and $B_{\rm z}^{(0)}$.

For a cylindrical flow geometry, and a steady–state flow of the form (56 – 60), the homogeneity of the linearized equations allows the perturbations to be decomposed into wave–like eigenfunctions

$$
\begin{aligned}
P^{(1)} &= P^{(1)}(r)\, e^{i(kz+n\theta-\omega t)} && (61)\\
\rho^{(1)} &= \rho^{(1)}(r)\, e^{i(kz+n\theta-\omega t)} && (62)\\
\mathbf{v}^{(1)} &= \mathbf{v}^{(1)}(r)\, e^{i(kz+n\theta-\omega t)} && (63)\\
\mathbf{B}^{(1)} &= \mathbf{B}^{(1)}(r)\, e^{i(kz+n\theta-\omega t)}. && (64)
\end{aligned}
$$

The spatial stability of the flow is described by the properties of the complex wave–number k, of the Kelvin–Helmholtz *normal modes* (61 – 64) for assumed real ω (Sec. 3.1). k and ω appear as eigenvalues of the solutions of the flow equations subject to the boundary conditions. General perturbations of the flow can be expressed as a superposition of these wavelike solutions provided that these solutions constitute a complete set of basis functions (see the discussion in Drazin & Reid 1981).

(61 – 64) imply that the Kelvin–Helmholtz normal modes are wavelike in z with wavenumber Re(k), wavelike in time with angular frequency ω, and develop $|n|$ oscillations around the circumference of the beam. The radial structure, specified by (for example) $P^{(1)}(r)$, dictates the extent to which these waves are localised near the beam. The azimuthal mode number, n, is a positive or negative integer, so that the eigenfunctions are single–valued, and the eigenfrequencies for positive and negative n are degenerate for the simplest beam configurations (non–rotating beams with only axial magnetic fields). For any given n, we expect the dispersion relation of (54) to describe a solution $k(\omega)$ (or a family of solutions) with similar azimuthal characteristics. $n = 0$ corresponds to a 'breathing' or 'pinching' mode of the beam, where the beam expands or contracts coherently at any z: only this mode causes the beam area to change. $n = \pm 1$ modes display sideways displacements of the beam with a helical pattern in z (these are the 'helical' or 'kink' modes): only these modes cause the beam centroid to be displaced. Modes with $|n| > 1$ (referred to as 'fluting' modes) produce distortions with ripples around the circumference of the beam—for $n = \pm 2$ there are two nodes on the beam surface.

The boundary conditions on the flow variables are imposed at $r \to \infty$ in the ambient medium, and at the boundaries between the ambient and sheared fluids (at $r = R_{\rm sa}$ before perturbation) and the sheared and beam fluids (at $r = R_{\rm bs}$ before perturbation). These conditions are

- all the flow variables should be finite at all r at finite t (including downstream from any z—see Sec. 3.1);
- all the flow variables should $\rightarrow 0$ as $r \rightarrow \infty$ at all finite time;
- the flow variables should be continuous functions of r;
- the radial phase velocity of the perturbations should be positive at $r \rightarrow \infty$ (so that perturbations are radiated from the beam);
- the radial displacements of the beam fluid and the ambient medium, $\xi_{\rm r}^{(1)}$, where

$$\frac{d\xi^{(1)}}{dt} = v_{\rm r}^{(1)}, \tag{65}$$

  should match at $r = R_{\rm bs}$ and $R_{\rm sa}$;
- the total (fluid plus magnetic) pressures should match at $r = R_{\rm bs}$ and $R_{\rm sa}$;
- the perpendicular (radial) component of the magnetic field should match at the boundaries; and
- the parallel component of the electric field should match at the boundaries.

For high $Re_{\rm m}$, conditions (g) and (h) imply that the magnetic field is continuous at the boundary. Note the relevance of the problem of the divergence of the flow at downstream infinity (condition b), and the use of the Sommerfeld finiteness and radiation conditions (a, b, and d) for the perturbations.

3.3.1. *Relativistic, non-magnetic beams*

It is fairly easy to derive the eigenfunction equation for the pressure perturbation for a relativistic, non-magnetic beam with a general velocity and density structure. The flow variables obey the usual equations of relativistic fluid flow (44 – 47). If the equilibria (56 – 60) and perturbations (61 – 64) are substituted for the flow variables and the equations are linearised, they can be manipulated into the form

$$\begin{aligned}
-i\omega\left(\gamma^{(0)^2}(\rho^{(1)} + \frac{P^{(1)}}{c^2}) - \frac{P^{(1)}}{c^2} + 2\gamma^{(0)^4}\frac{v_{\rm z}^{(0)}v_{\rm z}^{(1)}}{c^2}(\rho^{(0)} + \frac{P^{(0)}}{c^2})\right)& \\
+\frac{1}{r}\frac{d}{dr}\left(r\gamma^{(0)^2}(\rho^{(0)} + \frac{P^{(0)}}{c^2})v_{\rm r}^{(1)}\right) + \frac{in}{r}\gamma^{(0)^2}(\rho^{(0)} + \frac{P^{(0)}}{c^2})v_\theta^{(1)}& \\
+ik\left(\gamma^{(0)^2}v_{\rm z}^{(0)}(\rho^{(1)} + \frac{P^{(1)}}{c^2}) + \gamma^{(0)^4}(\rho^{(0)} + \frac{P^{(0)}}{c^2})(1 + \frac{v_{\rm z}^{(0)^2}}{c^2})v_{\rm z}^{(1)}\right) &= 0 \qquad (66) \\
i\gamma^{(0)^2}(\rho^{(0)} + \frac{P^{(0)}}{c^2})(kv_{\rm z}^{(0)} - \omega)v_{\rm r}^{(1)} + \frac{dP^{(1)}}{dr} &= 0 \qquad (67)
\end{aligned}$$

$$i\gamma^{(0)^2}(\rho^{(0)} + \frac{P^{(0)}}{c^2})(kv_{\rm z}^{(0)} - \omega)v_\theta^{(1)} + \frac{in}{r}P^{(1)} \;=\; 0 \quad (68)$$

$$i\gamma^{(0)^2}(\rho^{(0)} + \frac{P^{(0)}}{c^2})(kv_{\rm z}^{(0)} - \omega)v_{\rm z}^{(1)}$$
$$+\,\gamma^{(0)^2}(\rho^{(0)} + \frac{P^{(0)}}{c^2})\,v_{\rm r}^{(1)}\frac{dv_{\rm z}^{(0)}}{dr} + i(k - \frac{\omega v_{\rm z}^{(0)}}{c^2})P^{(1)} \;=\; 0 \quad (69)$$

$$i(kv_{\rm z}^{(0)} - \omega)\left(\frac{P^{(1)}}{P^{(0)}} - \Gamma\frac{\rho^{(1)}}{\rho^{(0)}}\right) - \frac{\Gamma}{\rho^{(0)}}\frac{d\rho^{(0)}}{dr}v_{\rm r}^{(1)} \;=\; 0 \quad (70)$$

where the final equation results from a model for the beam fluid in which the entropy is given by

$$s = s_0 + \frac{k_{\rm B}}{\Gamma - 1}\ln P\rho^{-\Gamma} \quad (71)$$

with s_0 and Γ, the polytropic index, being constants. This form for $s(P,\rho)$ should be adequate when $nk_{\rm B}T < \rho c^2$, but is, nevertheless, not sufficiently general for a relativistic fluid (see Synge, 1957).

(66 – 71) can be manipulated to yield a single, second–order, differential equation for the pressure perturbation,

$$\frac{d^2P^{(1)}}{dr^2} + \frac{dP^{(1)}}{dr}\left(\frac{1}{r} + 2\,\gamma^{(0)^2}\frac{(k - \frac{\omega v_{\rm z}^{(0)}}{c^2})}{(\omega - kv_{\rm z}^{(0)})}\frac{dv_{\rm z}^{(0)}}{dr} - \frac{\frac{d\rho^{(0)}}{dr}}{\rho^{(0)} + \frac{P^{(0)}}{c^2}}\right)$$
$$+P^{(1)}\left(\gamma^{(0)^2}\left(\frac{(\omega - kv_{\rm z}^{(0)})^2}{c_{\rm S}^2} - \left(k - \frac{\omega v_{\rm z}^{(0)}}{c^2}\right)^2\right) - \frac{n^2}{r^2}\right) \;=\; 0 \quad (72)$$

where $c_{\rm S}(r)$ is the local sound speed,

$$c_{\rm S} = \left(\frac{\Gamma P^{(0)}}{\rho^{(0)}}\right)^{1/2} \quad (73)$$

(Birkinshaw, 1984). Hardee (1984) has derived a similar equation for the pressure perturbation on an expanding beam.

Simple solutions of (72) for $P^{(1)}$ arise in the ambient medium and the beam core, where the density and velocity gradients vanish, since (72) then simplifies to Bessel's equation in αr, where the radial wavenumber

$$\alpha = \gamma^{(0)}\left(\frac{(\omega - kv_{\rm z}^{(0)})^2}{c_{\rm S}^2} - \left(k - \frac{\omega v_{\rm z}^{(0)}}{c^2}\right)^2\right)^{1/2}. \quad (74)$$

The pressure perturbation in $r > R_{\rm sa}$ which satisfies the boundary conditions is then

$$P^{(1)}(r) = \epsilon_{\rm a}P^{(0)}\frac{H_{\rm n}^{(1)}(\alpha_{\rm a}r)}{H_{\rm n}^{(1)}(\alpha_{\rm a}R_{\rm sa})} \quad (75)$$

where $H_{\rm n}^{(1)}(z)$ is a Hankel function of the first kind with order n. $\epsilon_{\rm a} \ll 1$ is a measure of the smallness of the pressure perturbation relative to $P^{(0)}$, and $\alpha_{\rm a}$ is given by (74) with $v_{\rm z}^{(0)} = 0$, $\rho^{(0)} = \rho_{\rm a}$, and $c_{\rm S} = c_{\rm Sa}$, the sound speed in the ambient medium. (75) represents an outward–going, decaying mode (a radiated sound wave) as $r \to \infty$, as required by boundary conditions (a – d).

In the unsheared beam core, the solution regular at $r = 0$ is

$$P^{(1)}(r) = \epsilon_{\rm b} P^{(0)} \frac{J_{\rm n}(\alpha_{\rm b} r)}{J_{\rm n}(\alpha_{\rm b} R_{\rm bs})} \tag{76}$$

where $J_{\rm n}(z)$ is a Bessel function of the first kind and order n. $\epsilon_{\rm b} \ll 1$ is a constant defining the smallness of the internal pressure perturbation, and the internal radial wavenumber, $\alpha_{\rm b}$, is given by (74) with $\rho^{(0)} = \rho_{\rm b}$, $v_{\rm z}^{(0)} = v_{\rm b}$, and $c_{\rm S} = c_{\rm Sb}$, the sound speed in the core. The beam-core solution is a standing pressure wave.

Finally, the pressure perturbation must be found in the sheared region ($R_{\rm bs} < r < R_{\rm sa}$) between the beam core and the ambient medium. The simplest choice is to assume that the beam core and ambient medium are in direct contact, at $R_{\rm bs} = R_{\rm sa} = R$. In this case, Ferrari *et al.* (1978), Hardee (1979), and others match the radial fluid displacements

$$\xi_{\rm r}^{(1)} = \frac{\frac{dP^{(1)}}{dr}}{{\gamma^{(0)}}^2 (\rho^{(0)} + \frac{P^{(0)}}{c^2})(\omega - k v_{\rm z}^{(0)})^2} \tag{77}$$

and the perturbed pressures, $P^{(1)}$, at the interface (as required by the boundary conditions) to obtain the dispersion relation

$$\begin{aligned} \mathcal{D}(k,\omega) &= \frac{H_{\rm n}^{(1)'}(\alpha_{\rm a} R)}{H_{\rm n}^{(1)}(\alpha_{\rm a} R)} \cdot \frac{\alpha_{\rm a}}{\omega^2 \, (\rho_{\rm a} + \frac{P^{(0)}}{c^2})} \\ &\qquad - \frac{J_{\rm n}'(\alpha_{\rm b} R)}{J_{\rm n}(\alpha_{\rm b} R)} \cdot \frac{\alpha_{\rm b}}{\gamma_{\rm b}^2 (\omega - k v_{\rm b})^2 \, (\rho_{\rm b} + \frac{P^{(0)}}{c^2})} \\ &= 0 \end{aligned} \tag{78}$$

where the primes ($'$) denote differentiation with respect to argument, and $\gamma_{\rm b}$ is the beam Lorentz factor. The essential character of the dispersion relation for a conical beam with small opening angle is the same (Hardee 1984, 1986).

It is clear from (75, 76, and 78) that the Kelvin–Helmholtz modes are sound waves associated with the beam/ambient medium interface. The growth rate of the instability is related to the extent to which these waves are localised in the beam or efficiently radiated, i.e., to the match between the wave impedances of the beam and ambient medium fluids as a function of frequency (Payne & Cohn 1985).

The use of a vortex sheet interface is beguilingly simple, and (78) is susceptible to detailed mathematical analysis, but several important points are lost by this choice. The shear layer around a supersonic beam contains the *critical surface* at which the speed of a Kelvin–Helmholtz mode equals the speed of the fluid flow. The nature of this critical surface plays an important role in the development of the instability in laboratory jets, and it represents the location of a regular singularity in the differential equation for $P^{(1)}$. A second rationale for a study of a shear layer is as a test of the assertion that shear layers are transparent to long–wavelength modes, but suppress short wavelength instabilities. This view may be an oversimplification, since the presence of shear may *destabilise* some modes at sufficiently high Mach number $\mathcal{M}_{\rm b} = v_{\rm b}/c_{\rm Sb}$ for shear layers which are not too wide.

The pressure perturbation in a linearly–sheared sheathing layer around a beam is

$$P^{(1)}(r) = \epsilon_{\rm s1}\, P^{(0)} \frac{F_{\rm n}^{(1)}(r)}{F_{\rm n}^{(1)}(R_{\rm bs})} + \epsilon_{\rm s2}\, P^{(0)} \frac{F_{\rm n}^{(2)}(r)}{F_{\rm n}^{(2)}(R_{\rm sa})} \qquad R_{\rm sa} > r > R_{\rm bs} \tag{79}$$

where $F^{(1)}$ and $F^{(2)}$ are independent solutions of (78) in the sheared layer, and can be expressed as infinite, convergent, series of terms or pairs of series (Birkinshaw, 1991). A dispersion relation $\mathcal{D}(\omega, k)$ similar to (78), but involving $F^{(1)}$ and $F^{(2)}$ as well as $J_{\rm n}$ and $H_{\rm n}^{(1)}$, can be deduced by matching the pressures and fluid displacements at $r = R_{\rm sa}$ and $r = R_{\rm bs}$.

Bodo *et al.* (1989) have extended the theory by including the effects of uniform rotation of the steady-state beam (adding a velocity component $v_\theta^{(0)} \propto r$). Their work has discussed only non–relativistic, $n = 0$ modes, and indicates the existence of a new channel of instability.

3.3.2. *Non-relativistic, magnetic beams*

The basic equations of fluid motion for an ideal, compressible, magnetic fluid in non–relativistic motion ($v \ll c$) are (48 – 53). Interpreting the fluid variables as a superposition of the steady–state equilibria defined by (56 – 60) and perturbations of the form (61 – 64), they may be reduced to a set of eight non–redundant equations in the perturbations, but these eight equations are too complicated for useful manipulation if general $v_{\rm z}^{(0)}(r)$, $\rho^{(0)}(r)$, $B_\theta^{(0)}(r)$ and $B_{\rm z}^{(0)}(r)$ are assumed.

A variety of treatments of these equations in different limits, or with different forms for the magnetic field distributions have been discussed. Cohn (1983) considered the stability of a magnetically–pinched beam of this type with a vortex boundary layer at $r = R$, no density or velocity gradients, and an azimuthal field $B_\theta^{(0)} \propto \frac{1}{r}$ for $n = 0$ modes only. In this limit a solution for the fluid perturbations can be obtained in terms of confluent hypergeometric functions. Ray (1981) studied a cylindrical plasma beam with an incompressible equation of state and uniform velocity, density, and internal magnetic field $B_{\rm z}^{(0)}$. Ferrari *et al.* (1981)

have discussed the stability of cylindrical flows of the same type, but with a relativistic beam velocity. Following the same methods as in Sec. 3.3.1, it is simple to manipulate (48 – 53) to obtain the non–relativistic analogue of Ferrari *et al.*'s governing equation for the pressure perturbation,

$$\frac{d^2P^{(1)}}{dr^2} + \frac{1}{r}\frac{dP^{(1)}}{dr} + P^{(1)}\left(\frac{\left(k^2 - \frac{(kv_{\rm z}^{(0)}-\omega)^2}{c_{\rm S}^2}\right)\left(\frac{(kv_{\rm z}^{(0)}-\omega)^2}{c_{\rm A}^2} - k^2\right)}{\left(k^2 - (kv_{\rm z}^{(0)}-\omega)^2\,(\frac{1}{c_{\rm A}^2}+\frac{1}{c_{\rm S}^2})\right)} - \frac{n^2}{r^2}\right) = 0 \quad (80)$$

which is a form of Bessel's equation. The solution for $P^{(1)}$ can be written

$$P^{(1)}(r) = \begin{cases} \epsilon_{\rm a} P_{\rm a} \frac{H_{\rm n}^{(1)}(\alpha_{\rm a} r)}{H_{\rm n}^{(1)}(\alpha_{\rm a} R_{\rm sa})} & r > R_{\rm sa} \\ \epsilon_{\rm b} P_{\rm b} \frac{J_{\rm n}(\alpha_{\rm b} r)}{J_{\rm n}(\alpha_{\rm b} R_{\rm bs})} & r < R_{\rm bs} \end{cases} \quad (81)$$

where the radial wavenumbers are given by

$$\alpha = \left(\frac{\left(1 - \left(\frac{\omega - kv_{\rm z}^{(0)}}{kc_{\rm S}}\right)^2\right)\left(\left(\frac{\omega - kv_{\rm z}^{(0)}}{kc_{\rm A}}\right)^2 - 1\right)}{1 - \left(\frac{\omega - kv_{\rm z}^{(0)}}{kc_{\rm A}}\right)^2\left(1 + (\frac{c_{\rm A}}{c_{\rm S}})^2\right)}\right)^{1/2} \quad (82)$$

with sound speed $c_{\rm S} = c_{\rm Sa}$ or $c_{\rm Sb}$, Alfvén velocity $c_{\rm A} = c_{\rm Aa}$ or $c_{\rm Ab}$, density $\rho^{(0)} = \rho_{\rm a}$ or $\rho_{\rm b}$, flow velocity $v_{\rm z}^{(0)} = 0$ or $v_{\rm b}$, and pressure $P^{(0)} = P_{\rm a}$ or $P_{\rm b}$ for the ambient and beam wavenumbers, $\alpha_{\rm a}$ and $\alpha_{\rm b}$, respectively. The condition of transverse pressure equilibrium is then

$$P_{\rm a} + \frac{B_{\rm za}^2}{2\mu_0} = P_{\rm b} + \frac{B_{\rm zb}^2}{2\mu_0}, \quad (83)$$

and for a vortex layer boundary (associated with a current sheet) the dispersion relation becomes

$$\begin{aligned} \mathcal{D}(k,\omega) &= \frac{H_{\rm n}^{(1)\prime}(\alpha_{\rm a}R)}{H_{\rm n}^{(1)}(\alpha_{\rm a}R)}\cdot\frac{\alpha_{\rm a}}{\rho_{\rm a}}\cdot\frac{1}{\omega^2 - k^2c_{\rm Aa}^2} \\ &\qquad - \frac{J_{\rm n}'(\alpha_{\rm b}R)}{J_{\rm n}(\alpha_{\rm b}R)}\cdot\frac{\alpha_{\rm b}}{\rho_{\rm b}}\cdot\frac{1}{(\omega - kv_{\rm b})^2 - k^2c_{\rm Ab}^2} \\ &= 0. \end{aligned} \quad (84)$$

The Kelvin–Helmholtz modes are magnetosonic waves partially trapped in the beam cavity. Note that Ferrari *et al.*'s (1981) treatment is more general than that given above, since it includes the effects of relativistic beam motion.

Another version of (84), incorporating the effects of uniform beam rotation, was derived by Bodo *et al.* (1989). Fiedler & Jones (1984) considered a beam carrying a uniform current density, with both axial and azimuthal fields, bounded by a vortex sheet, and with no gradients in density or velocity, and derived the properties of the unstable modes numerically (since no analytic dispersion relation could be found). A further modification of the theory by Trussoni *et al.* (1988) considers the effect of allowing the fluid pressure to be anisotropic, with independent components parallel and perpendicular to an axial magnetic field inside the beam. No qualitatively-new features appear for fast beams, but flows with low Mach numbers tend to become unstable.

3.4. The form of the instability

A dispersion relation such as (78) or (84) is analysed from a spatial viewpoint by solving for complex k as a function of real ω. The wavelength and growth length of the instabilities are then

$$\lambda_0 = \frac{2\pi}{\mathrm{Re}(k)} \tag{85}$$

$$\lambda_\mathrm{e} = -\frac{1}{\mathrm{Im}(k)} \tag{86}$$

and the pressure perturbation grows with distance down the beam, z, as e^{z/λ_e}. If many instability modes are active, then it is usually assumed that the fastest–growing mode (of wavelength λ_0^* and growth length λ_e^*) dominates the flow after a short incubation period (of length a few λ_e^*). Thus the dispersion relations are searched for the values of ω and n that produce the minimum value for λ_e^*, when the stability of the beam is described by this value, and the shape of the deformed beam is described by the corresponding eigenmode.

A spatial analysis of the shear-protected beam has been given by Birkinshaw (1991), and curves of $\lambda_\mathrm{e}(\lambda_0)$ for several beams are shown in Figs 13 – 20, where the instability curves are drawn for azimuthal mode numbers $n = 0$ (the "pinching" modes, drawn with solid lines), $n = 1$ (the "helical" modes, drawn with dashed lines), and $n = 2$ (the first "fluting" modes, drawn with dot-dashed line). For each value of n the curve may show many branches. These branches have been labelled by N, the radial mode number, which represents the number of nulls in the pressure perturbation in $0 < r < R$. $N = 0$ modes are the 'Ordinary Modes' and $N > 0$ modes are the 'Reflection Modes' of Gill (1965) and Ferrari *et al* (1981). Reflection modes appear only for sufficiently large beam velocity (if $v_\mathrm{b} > c_\mathrm{Sa} + c_\mathrm{Sb}$; Payne & Cohn 1985); at smaller v_b only the ordinary mode is present. Analytical approximations for the values of λ_0^* and λ_e^* are given by Hardee (1987a, b) for low–n and low–N modes, and by Zaninetti (1986a, b) for short-wavelength modes in magnetic beams.

For beams which support reflection modes, Figs 13 to 18 show that many modes can be excited at sufficiently small wavelength, λ_0. For example, at $\lambda_0 = 10R$ in a beam with Mach number $\mathcal{M}_\mathrm{b} = 10$ and $\rho_\mathrm{a} = \rho_\mathrm{b}$ (Fig. 13), modes with $n = 0$,

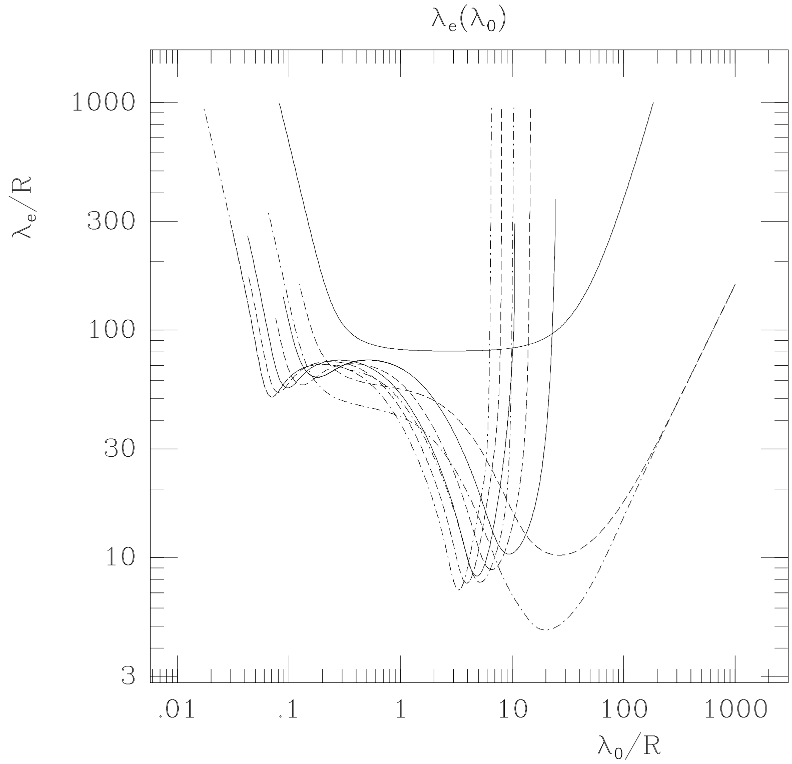

Fig. 13. The mode structure for a beam velocity 3000 $\mathrm{km\,s^{-1}}$, density equal to the density of the ambient medium, and internal sounce speed 300 $\mathrm{km\,s^{-1}}$, bounded by a vortex sheet ($\delta = 0$). The ordinary modes extend to large λ_0, with the $n = 1$ and $n = 2$ modes degenerate at large λ_0 and the $n = 0$ mode more stable. The reflection modes appear at $\lambda_0 < 25R$, and have sharper minima than the ordinary modes. Many further reflection modes extend to shorter wavelengths, and are more unstable than the shortest-wavelength reflection mode appearing here (which has $n = 2$, $N = 2$).

$N = 0, 1, 2$, with $n = 1$, $N = 0, 1$, and with $n = 2$, $N = 0, 1$ are excited (as well as all modes with $n > 2$ and $N = 0$). If only modes of this wavelength and $n < 3$ are accessible to the beam then the $n = 2$, $N = 0$ mode, which has the smallest growth length, $\lambda_e \approx 7R$, would dominate the structure of the beam and should be visible to observers. Since there is no reason to suspect that $\lambda_0 = 10R$ is the only wavelength that is excited on the beam, Fig. 13 suggests that the fastest–growing mode tends to be that of smallest wavelength and largest n (the cylindrical analogue of the result obtained for a planar shear layer by Turland & Scheuer 1976). Even for a beam protected by a shear layer (Fig. 14), this theory does not

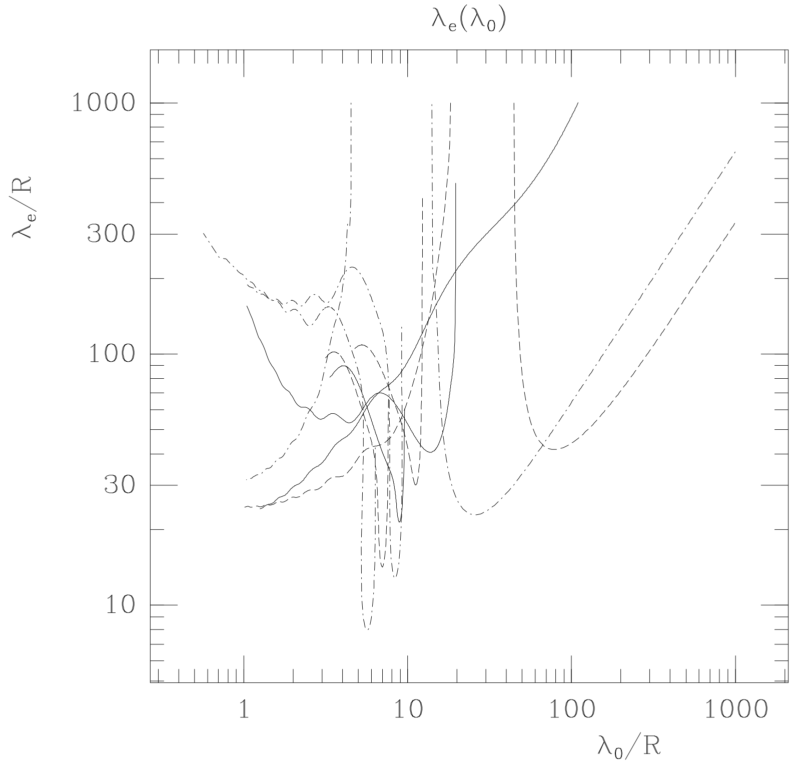

Fig. 14. The mode structure for the beam shown in Fig. 13, but now bounded by a shear layer with $\delta = 1$. The reflection modes are similar, except that they show ripples at the short wavelengths, and the regions of peak instability are slightly sharper, because of resonances with shear-layer modes. The ordinary modes are more severely modified, with the $n = 1$ and $n = 2$ modes now showing regions of stability at $\lambda_0 \approx 20R$, while the $n = 0$ mode is destabilised at short wavelengths.

predict an unambiguous mode which dominates the instability of a beam—rather we must appeal to other physical principles to set the ranges of ω and n which are accessible to instabilities, and then locate the values of λ_0^* and λ_e^* given this range. However, as n increases the ordinary ($N = 0$) mode has a smaller growth length than an increasing number of reflection ($N > 0$) modes. High–n and N modes are unlikely to have a significant individual effect on a beam, although their effective *continuum* at small wavelengths may cause a smooth beam profile to develop by broadening the vortex layer to create a hot, sheared, sheathing layer that will inhibit the further growth of small–λ_0 instabilities.

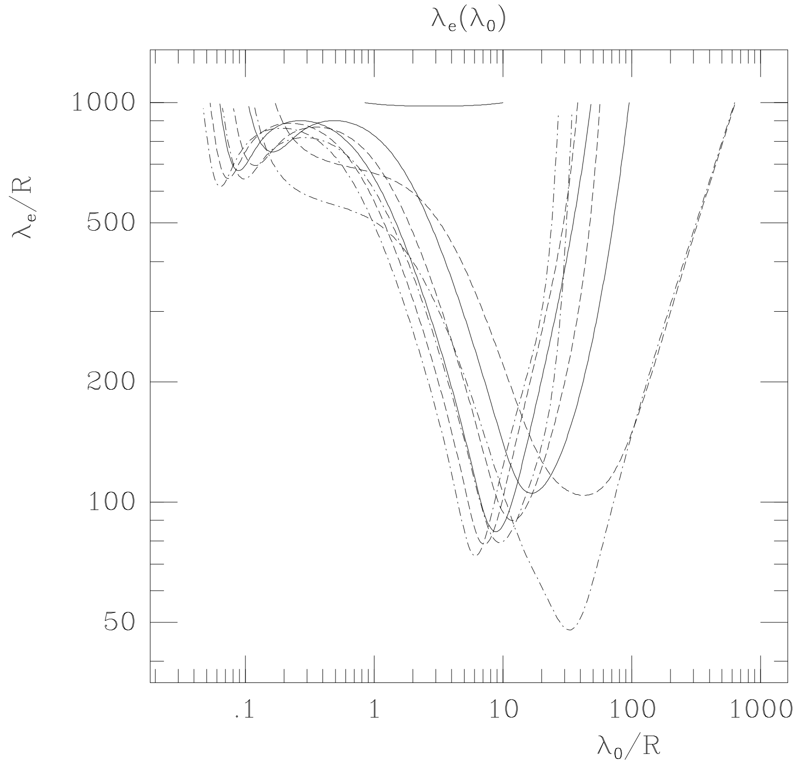

Fig. 15. Solutions of the dispersion relation (78) for a beam with velocity 3000 km s^{-1}, density 100 times the density of the ambient medium, and ambient medium sound speed 300 km s^{-1}, bounded by a vortex sheet ($\delta = 0$). The ordinary modes extend to large λ_0, with the $n = 1$ and $n = 2$ modes degenerate at large λ_0 and the $n = 0$ mode much more stable (so that it only appears on this plot near $\lambda_e = 10^3 R$). The reflection modes appear at $\lambda_0 < 100R$. Many higher-order reflection modes have been excluded from this plot, for clarity of presentation.

Figs 13 to 20 demonstrate that the spatial instability of low–density beams is greater than that of high–density beams with the same velocity, and that the overall stability of a beam is increased as the Mach number $\mathcal{M}_b$ is increased, but the growth lengths of pinching ($n = 0$) modes increase faster then the growth lengths of helical ($n = 1$) modes (Ray, 1981). This suggests that beams tend to display knots at small Mach numbers and tend to twist at high Mach numbers. The figures also show that the growth lengths of the dominant instabilities are small unless the beam is supersonic both internally and externally (*i.e.*, $v_b > c_{Sa}$ and $v_b > c_{Sb}$). Thus the condition that the instability growth lengths $\lambda_e > R$ for wavelengths $\lambda_0 > R$ is just the condition that the beam is supersonic, and

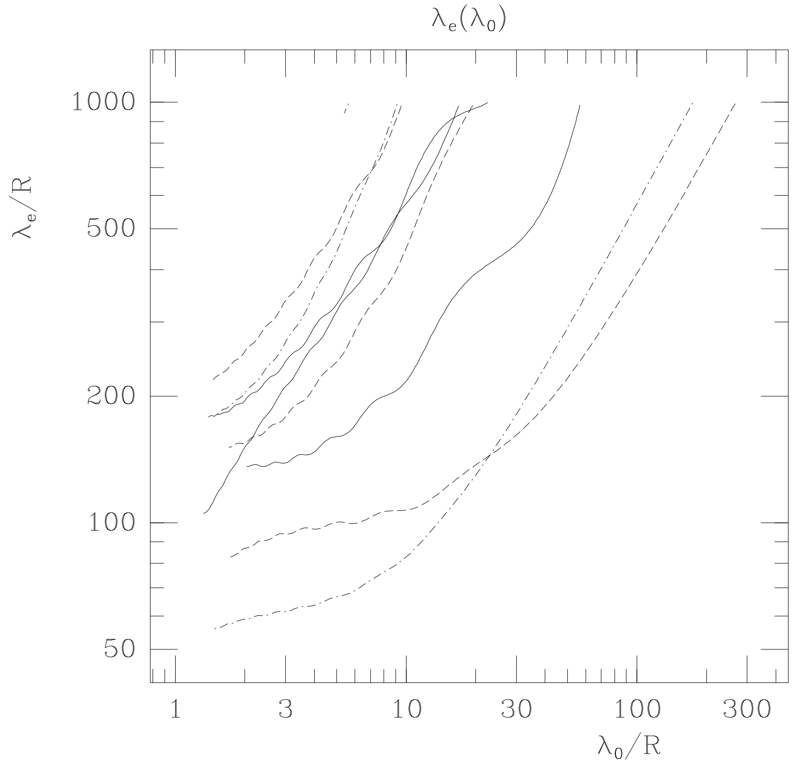

Fig. 16. The mode structure for the beam seen in Fig. 15, but now bounded by a shear layer with $\delta = 1$. The stability curves show ripples at over the full range of wavelengths, due to resonances with modes in the shear layer, and the ordinary and the reflection modes all have similarly-shaped stability curves without pronounced minima. The growth lengths of these instabilities are large, and the beam is fairly stable.

hence that its stability is dominated by reflection modes at short wavelengths and ordinary modes at long wavelengths (as in Fig. 13). It may be concluded that if the observed structures in radio jets are caused by the Kelvin–Helmholtz instability, then the beams are supersonic, and that the influence of the shortest–wavelength modes on the gross structure of the beam has been slight.

If the density of a beam is increased whilst the kinetic energy flux and the internal pressure are held constant, the velocity, $v_{\rm b}$, and the internal sound speed, $c_{\rm Sb}$, of the flow decrease. The combined effect of these changes is that the growth lengths $\lambda_{\rm e}^*$ of the modes increase slightly, and that the wavelengths λ_0^* increase faster (if $\rho_{\rm b} > \rho_{\rm a}$) as functions of $\rho_{\rm b}$. An exception arises for the $n = 0$, $N = 0$ mode, which is destabilised. If the density of the beam is increased whilst the

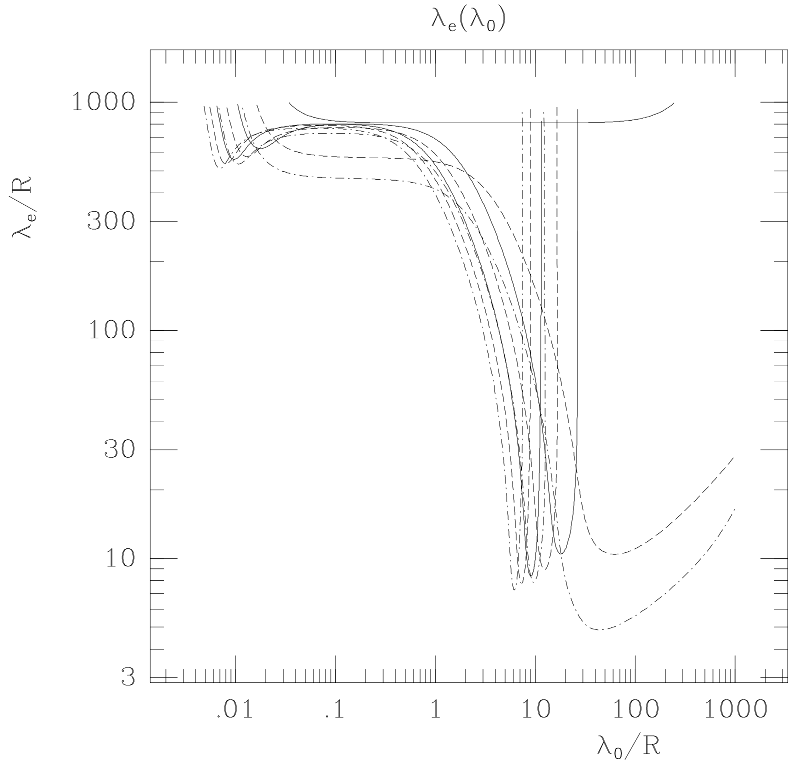

Fig. 17. Solutions of the dispersion relation (78) for a beam with velocity 3000 km s^{-1}, density 10^{-2} times the density of the ambient medium, and internal sound speed 300 km s^{-1}, bounded by a vortex sheet ($\delta = 0$). The ordinary modes extend to large λ_0, with the $n = 0$ mode (which appears near $\lambda_e = 10^3 R$) much more stable than the $n = 1$ and $n = 2$ modes. The reflection modes appear at $\lambda_0 < 28R$, and have sharper minima than the the ordinary modes. Many high-order modes have been excluded from this plot.

momentum flux is held constant, only small changes in the values of λ_e^* and λ_0^* result, except that the $n = 0$, $N = 0$ mode is destabilised again. A sufficiently large increase or decrease of ρ_b subject to either a fixed kinetic energy flux or momentum flux may cause v_b to decrease below $c_{Sa} + c_{Sb}$, so that the reflection modes no longer appear.

The pressure perturbations $P^{(1)}(r)$ for the $n = 2$, $N = 1$ modes of Figs 13 and 14 near maximum instability are illustrated in Figs 21 and 22. These perturbations are seen to have an appreciable amplitude over a significant region inside and outside the beam, although $P^{(1)}$ tends to zero as $r \to 0$ for $n > 0$. The ordinary mode ($N = 0$) is a consequence of the existence of any boundary between a flowing

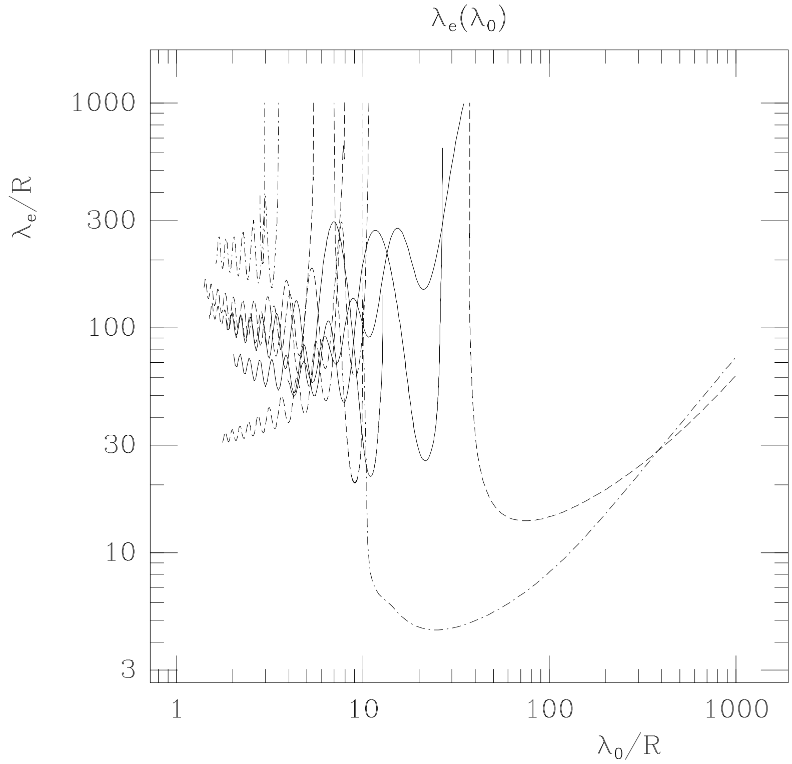

Fig. 18. The mode structure for the beam seen in Fig. 17, but now bounded by a shear layer with $\delta = 1$. The stability curves show dramatic ripples at short wavelengths for all the modes, caused by strong resonances with waves in the shear layer, and the $n = 1$ and $n = 2$ ordinary modes are absolutely stabilised at wavelengths $\lesssim 35R$ and $12R$, respectively. The zones of instability terminate after the wavelengths have dropped by a factor ≈ 4, when the ordinary modes lie in the same zone of strong resonances as the reflection modes. Note the $n = 2$ ordinary mode is much the most unstable, dominating the stability of the beam for wavelengths from $10 - 400R$. The first few reflection modes also show stabilised regions in this beam, so that the maximum wavelengths λ_0 at which they appear are smaller than would be expected.

and a static region of a fluid—it arises for planar flows (*e.g.*, Blake 1972; Turland & Scheuer 1976) as well as in other geometries, and is unstable for all wavelengths. Reflection ($N > 0$) modes, on the other hand, require the fluid to contain more than a single planar surface, and are particularly strong where the fluid contains an enclosed region whose walls can vibrate coherently (*e.g.*, the beam–cavity). In that case, instabilities occur as sound waves radiated from one surface are reflected back from the other surface (with some phase delay) to interfere constructively. Thus the beam acts as an acoustic waveguide: standing waves across the waveguide

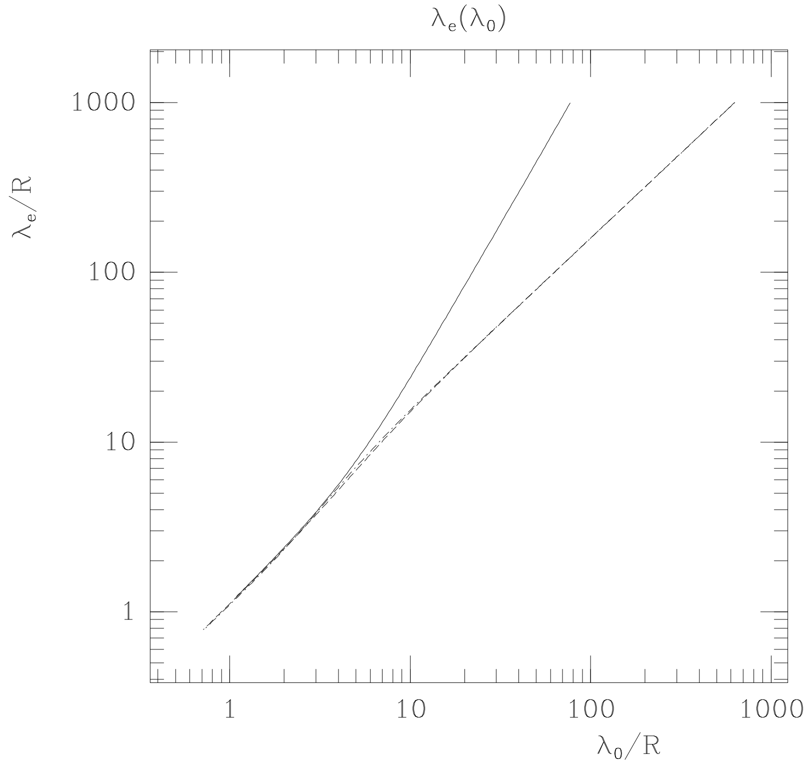

Fig. 19. Solutions of the dispersion relation (78) for a beam with velocity 3000 km s^{-1}, density 100 times the density of the ambient medium, and internal sound speed 300 km s^{-1} with a vortex layer boundary. Since $v_b < c_{Sa} + c_{Sb}$ for this beam, no reflection modes will appear. The stability curves are drawn with solid, dashed, and dot-dashed lines for $n = 0$, 1, and 2, respectively. The $n = 0$ mode is more stable than the $n = 1$ and $n = 2$ modes at large wavelength, and all three modes become degenerate and of the form $\lambda_e \propto \lambda_0$ as $\lambda_0 \to 0$, as would be found for a slab jet.

allow co–operative modes of the walls to be excited, and growing perturbations can be produced if the reflection coefficient for a wave striking a wall is greater than unity (over–reflection; Payne & Cohn 1985; Bodo *et al.* 1989). The appearance of reflection modes at regular intervals of λ_0 in Figs 13 to 18 can be interpreted in terms of this frequency–dependent coupling of internal modes of the beam to radiated magnetosonic waves (Bodo *et al.* 1989). A regular pattern of appearance of such modes as λ_0 is decreased corresponds to the 'fitting in' of increasing numbers of nulls of the pressure perturbation within the beam.

The presence of a shear layer around a beam complicates the instability pattern by allowing resonances within the shear layer itself. Various treatments of this

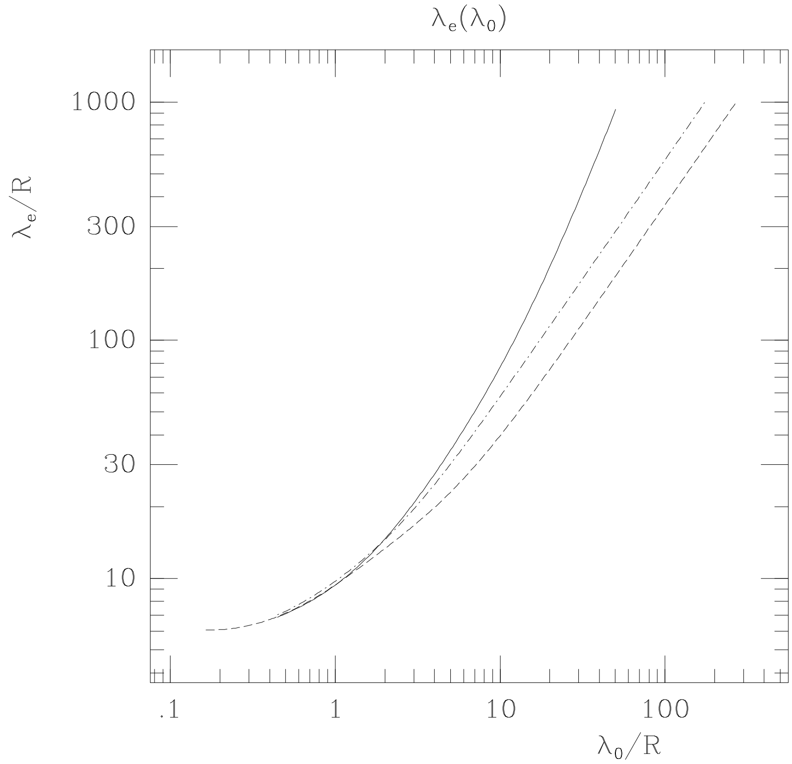

Fig. 20. The mode structure for the beam seen in Fig. 19, but now bounded by a shear layer with $\delta = 1$. The modes are stabilised at all wavelengths, but remain of the form $\lambda_e \propto \lambda_0$ at the longest wavelengths. As $\lambda_0 \to 0$, they become degenerate again, because the radial wavelengths become much smaller than R. As is usual for subsonic and transsonic beams, the flow is highly unstable to short-wavelength perturbations.

effect have been performed: by Ray (1982), Ferrari *et al.* (1982), Roy Choudhury & Lovelace (1984), and Hardee (1982, 1983, 1984). Earlier work on the structures of instabilities in shear layers has been done for laboratory jets by Blumen *et al.* (1975) and Drazin & Davey (1977). The solutions for a cylindrical beam bounded by linear shear layers, shown in Figs. 13 to 20 were obtained by Birkinshaw (1991).

The shear layer resonances modify the appearance of the vortex sheet modes by introducing additional structure into the $\lambda_e(\lambda_0)$ relation. In Fig. 14, for example, this can be seen as the additional "ripples" on the curves at small δ. As the dimensionless thickness of the shear layer, δ, is increased, the ordinary modes are slightly stabilized at long wavelengths. For wavelengths near the beam radius, R,

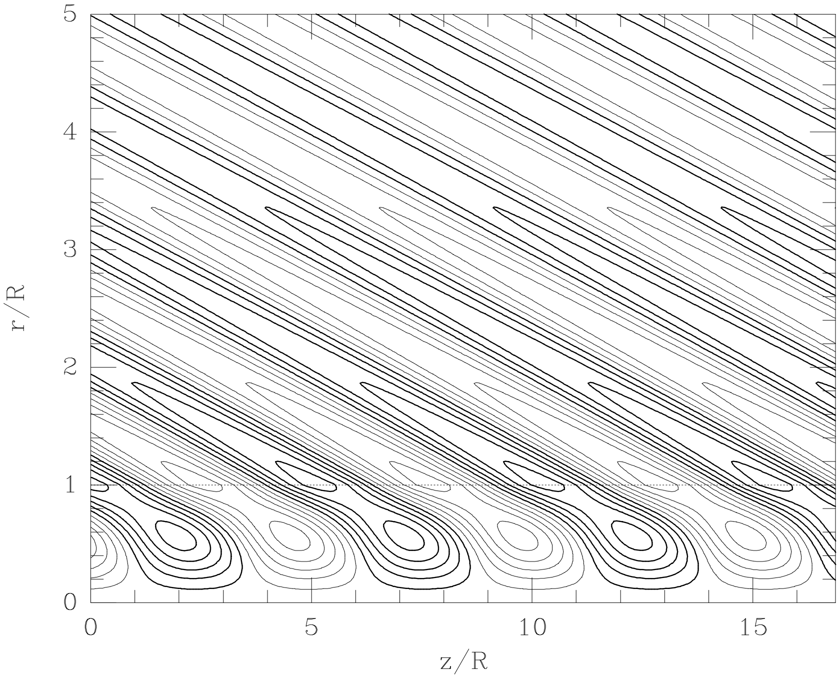

Fig. 21. The physical pressure solution, $\mathrm{Re}(P_1(r,\theta,z))$, for the $n = 2$, $N = 1$ mode at its maximum instability of the beam shown in Fig. 13 at a particular time, t. The dotted line represents the location of the vortex sheet, and contours of the pressure perturbation are drawn at equal intervals of $0.2\times$ the maximum pressure perturbation from -0.9 to $+0.9\times$ the maximum pressure perturbation in this region of the flow. Thicker lines mark the positive contours. For clarity, the exponential growth in the mode (for which $\lambda_e = 7.8R$) has been suppressed in this diagram. Note that the wave-train is inclined at an an angle $\approx 80^\circ$ to the beam axis in the ambient medium.

and at moderate δ, mode mixing causes slightly *greater* ordinary mode instability than in a vortex layer. The reflection modes are stabilised by the effects of the shear, and the wavelengths at which they appear, $\lambda_0^{\mathrm{crit}}$, change slightly. Large values of δ cause increasing stabilisation of the flow, and at sufficiently large δ some of the ordinary modes which are unstable for flows bounded by a vortex sheet become stable over a wide range of λ_0.

At the shortest wavelengths, even the presence of a wide shear layer does not cause complete mode stabilization, and it is precisely these short-wavelength modes that have the shortest growth lengths, and hence which should dominate beam instability.

Magnetic effects have been discussed by Cohn (1983), Ray (1981), Fiedler & Jones (1984), Ferrari *et al.* (1980, 1981) and by Benford (1981) for a cold beam (with no internal dynamics). Bodo *et al.* (1989) have discussed the stability of a rotating beam to the pinching ($n = 0$) mode. Roy Choudhury & Lovelace (1986)

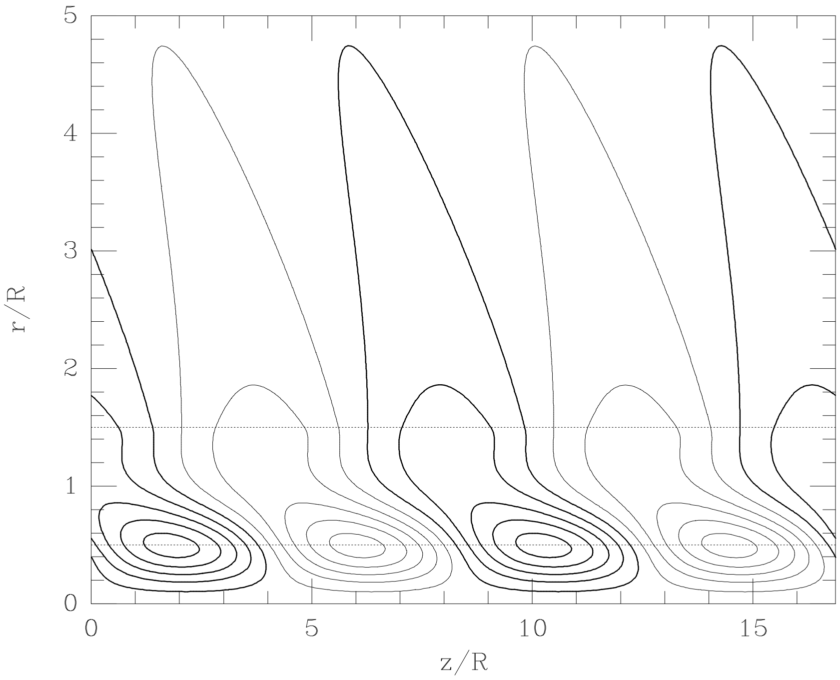

Fig. 22. The physical pressure solution, $\mathrm{Re}(P_1(r, \theta, z))$, for the $n = 2$, $N = 1$ mode at its maximum instability of the beam shown in Fig. 14 at a particular time, t. Dotted lines represent the inner and outer edges of the shear layer, and contours of the pressure perturbation are drawn at equal intervals of $0.2\times$ the maximum pressure perturbation from -0.9 to $+0.9\times$ the maximum pressure perturbation in this region of the flow. Thicker lines mark the positive contours. For clarity, the exponential growth in the mode (for which $\lambda_e = 12.8R$) has been suppressed in this diagram. Note that the wave-train is inclined at an an angle $\approx 45°$ to the beam axis in the ambient medium, and is more oblique (at an angle $\approx 70°$ to the beam axis) in the shear layer.

and Ray & Ershkovich (1983) have discussed the combined effects of magnetic field and shear on a planar flow. The results of these investigations are that all modes are stable for sub–Alfvénic flows ($v_b < c_{Ab}$) and axial magnetic fields (Ray 1981; Ferrari *et al.* 1981; Fiedler & Jones 1984). $n = 1$ modes stabilise at a lower axial field ($c_{Ab} > 0.5v_b$). By contrast, azimuthal fields are destabilising (as shown for the $n = 1$ modes by Ferrari *et al.* 1981; for the $n = 0$ and 1 modes by Fiedler & Jones 1984; and for $n = 0$ modes on magnetically–confined beams by Cohn 1983). In all cases, the nature of the instability is similar to that of a non–magnetic flow, and the rates of growth of instabilities are not much different from those of non–magnetic flows for axial fields less than the critical value for stabilisation,

$$B_{zb}^{\mathrm{crit}} \approx (n/\mathrm{m}^{-3})^{1/2}(v_b/c) \quad \mathrm{nT}. \tag{87}$$

None of the above discussions of the stability of magnetic beams identified the presence of slow magnetosonic reflection modes in the dispersion relation, but discuss only the ordinary modes and fast magnetosonic reflection modes. Bodo *et al.* (1989) have described the importance of the slow magnetosonic modes. Only ordinary modes are present at low (subsonic) beam speeds, the slow magnetosonic reflection modes dominate the stability next, and at high Mach numbers it is the fast magnetosonic relection modes that determine the stability of the flow.

The effect of Kelvin–Helmholtz modes on the *survival* of the beam cannot be predicted with certainty from the simple linear instability results—since small–λ_0 modes are the most unstable it is likely that the structure of the beam will adjust to suppress these modes before growth of the longer (λ_0, λ_e) modes (which may produce observable structures). The rapid adjustment of the structure of the beam to small–wavelength modes may invalidate the assumed z–independence of the flow used to derive the dispersion relations. Where longer wavelength modes occur, they should grow on a modified beam structure. The results of simple shear–layer calculations tend to suggest that the modification of the structure of the beam can be ignored in predicting the instability at long wavelengths. If we assume that the shorter–wavelength modes saturate by establishing a thin shear layer, then the shear–layer calculations of Ray (1981), Ferrari *et al.* (1982) and Birkinshaw (1991) suggest that the dominant instabilities will always be those with wavelengths comparable with the width of the shear layer. Since the width of the shear layer that is produced is not known, it is not possible to predict which wavelengths will dominate the stability of a given beam. The best use of the theory in its present state is, therefore, to attempt a consistency check between the wavelengths and growth lengths for modes which are inferred from maps of sources with the values that are predicted using jet parameters determined in other ways.

The linear calculations described above contain no information on the limits to the amplitudes of instability. The method that was used to derive the dispersion relations can be extended to second order, by writing the pressure (for example) as

$$P = P^{(0)}(\mathbf{r}, t) + P^{(1)}(\mathbf{r}, t) + P^{(2)}(\mathbf{r}, t), \tag{88}$$

and carrying the expansion of (44 − 47) or (48 − 53) to second order to obtain equations linear in $P^{(2)}$ (but quadratic in $P^{(1)}$), and then the behaviour of $P^{(2)}$ might yield limits to the growth of the instability. The analytical difficulties in performing such a calculation are severe, and no direct analytical discussion of the limits to growth has been made. Benford (1981) argues that the growth of the perturbations will cease when the velocity excursions produced by the Kelvin–Helmholtz modes become sonic and develop shocks—at $|\mathbf{v}^{(1)}| = c_{\mathrm{S}}$. This may be regarded as a strong upper limit on the linear phase of growth.

An alternative approach is to use numerical simulations of beams (*e.g.*, Nepveu 1982a, 1982b; Norman *et al.* 1982, 1983, 1984; Williams & Gull 1984) to discover the results of the growth of the instability. Norman *et al.* (1984) have examined their results in the light of analytical instability theory, and conclude that pinch reflection modes (with $n = 0$ and $N > 0$) do not have a significant effect in disrupting beams since their non–linear growth saturates with a series of weak conical shocks which cause alternate divergence and refocussing of the flow (that is, the growth of the pinch reflection modes terminates by Benford's (1981) sonic criterion). Recent calculations on slab beams (which can model the $n = 0$ and $n = 1$ modes of cylindrical beams) by Hardee & Norman (1988) and Norman & Hardee (1988) indicate that the reflection modes saturate with the formation of weak oblique shocks, whilst the ordinary modes are unsaturated and can cause large-scale distortions and disruption of the flow. Since the ordinary pinching mode is only important for trans–sonic flows, this suggests that the ordinary helical mode may be the most important long-wavelength instability channel for supersonic beams. The numerical simulations found growth lengths $\lambda_e^* = (2-4)\mathcal{M}_b R$ and wavelengths $\lambda_0^* \approx 5R$ for Mach numbers $\mathcal{M}_b = 3$ to 6, in fair agreement with linear instability theory.

It is easy to see from Figs. 13 to 20 that low–density beams are expected to make a rapid transition to turbulence since their short–wavelength modes have growth lengths less than R. Higher sound–speeds in the ambient medium and the beam ameliorate this situation as far as the low–order reflection modes are concerned, but the higher–order modes will still have small values of λ_e^*. The transition to turbulence can only be prevented if the beam is well protected from the influence of modes with wavelengths less than a few R—such protection might be provided by a hot sheathing layer for which waves with $\lambda_0 < \delta R$ will propagate poorly. Beams which are more dense then the ambient medium are rather stable and only slightly affected by short wavelength modes (until the frequency of the driving perturbation becomes very high—that is, until the wavelength of the driving mode becomes much less than the beam radius). For simple beam structures, therefore, the single clear prediction of Kelvin–Helmholtz theory is that light beams will make a fast transition from laminar to turbulent flow, whilst denser beams can remain laminar longer.

3.5. The structure of a distorted beam

The growth of the modes described above may lead to observable distortions on a beam if the wavelengths and growth lengths are not severely modified in their transition from the linear to the non–linear phase of growth, and if the beams are not first disrupted by the influence of the shortest wavelengths of instability. In this Section we apply the results of an analysis of sheared beams to models of 3C 449, NGC 6251, and HH 34 assuming that magnetic fields are not dynamically important and do not suppress the Kelvin-Helmholtz modes.

Since the result of the operation of Kelvin–Helmholtz modes, as observed in the laboratory, is the transition to turbulence of the beam flow, it is logical to interpret the greater or lesser instability of astrophysical beams as an indication of their susceptibility to turbulence. Ferrari *et al.* (1979) suggested that the radio–bright jets that are common in low–power radio galaxies and high–power quasars are indicative of turbulent particle acceleration occurring in beams which are very unstable, and that the 'invisible' jets of the higher–power radio galaxies should be interpreted as beams which are more stable, and hence have not developed strong turbulence and its consequent particle acceleration. Since light beams are more unstable than dense beams, it might be suggested that this tendancy to bright radio emission might also be taken as a tracer of beam density, but there is no independent evidence for this hypothesis.

For an identification of the mode structures with the radio morphologies to be possible, a number of assumptions are necessary:

- that the observed radio structures trace the actual fluid flow carrying energy from the galaxy to the outer parts of the radio source;
- that the wavelengths and growth lengths of the unstable modes are not severely modified in their transition from the linear to the non–linear phase of growth, so that the forms of $P_1(r)$ reflect the observable distortions; and
- that the beams are not disrupted by very short wavelength modes (with $\lambda_0 \ll R$), which are usually the modes that grow most rapidly.

Since typical modes of instability involve appreciable pressures over the entire volume of the beam and of the shear layer (Figs 21 and 22), edge brightening of the beam is not to be expected if the radio brightness is related to the pressure perturbation through particle acceleration, or if the diffusion of relativistic electrons in the beam is efficient (as might be the case if the magnetic field in the beam is tangled; e.g., Eilek 1982. Note that even the dynamically-unimportant fields that are consistent with the present treatment of a beam as a field-free flow may still dominate the diffusion of relativistic electrons.) Observationally, there is little evidence for the presence of limb–brightening, except in circumstances like the first knot in the Cen A radio jet (Clarke *et al.*, 1986a) where it is clear that complicated flow phenomena are occurring. Although the result that distorted beams show no limb brightnening is in accord with the predictions of the Kelvin–Helmholtz model, this is also a feature of other models for beam–bending. It should be stressed that the effects of projection can cause complicated patterns to be seen from simple beam structures (Zaninetti & Van Horn 1988), so that the relative orientation of the beam and the line of sight is of critical importance in interpreting the jet structures. Furthermore, the assumption that the pressure perturbation is simply related to the radio brightness of the beam is certainly unjustified: no convincing discussion of beam appearance with a realistic particle acceleration model has been produced.

3.5.1. *Application to 3C 449*

3C 449 (Sec. 1.2.4) is the archetypal distorted radio jet for which most comparisons between the structure and the Kelvin-Helmholtz instability model (and other models; e.g. Blandford & Icke 1978; Wirth *et al.* 1982) have been made. Hardee (1981) interpreted the large side-to-side oscillations in the radio structure of this two–sided jet in terms of a beam affected by an $n = 1$ Kelvin–Helmholtz mode with $\lambda_0 \approx 16R$ and $\lambda_e \approx 6R$ in a beam with Mach number $\mathcal{M}_b = 10$, and equal densities in the beam and the ambient medium. Assuming that the observed non-linear structure of 3C 449's jet reflects the linear mode structure imposed by the initial growth of Kelvin-Helmholtz modes, we can use the results of Figs 13 and 14 to discuss the structure of the flow.

In Figs 13 and 14 we see that the shortest growth length of the $n = 1$ ordinary mode in a $M_b = 10$, equal-density, beam varies from about $10R$ to about $42R$ as the width of a sheathing layer is increased from 0 to R. At the same time, the wavelengths of the modes increase from about $27R$ to about $79R$. To obtain agreement with the structure of the jet in 3C 449, the direction of the jet must be inclined at an angle of about 50 degrees to the plane of the sky and the shear layer in 3C 449 must be thin, since a thick shear layer causes the growth length to be too large relative to the wavelength.

The $n = 1$ reflection modes can also produce helical waves on the beam, since they have the appropriate θ-symmetry to deflect the centre line of the flow, but for $M_b = 10$, all these modes have wavelengths that are too small to produce the observed structure of 3C 449, whether or not the beam is sheathed. Thus if the beam in 3C 449 has $M_b = 10$, and a density equal to that of the external medium, the observed wiggles are produced by the Kelvin-Helmholtz instability only if the edge of the jet is sharp.

This conclusion can be avoided if the observed width of the radio emission in the radio jet of 3C 449 does not reflect the width of the underlying beam—perhaps particle diffusion causes the radio emission to come from a much larger radius than the beam-core or beam-core plus shear layer. In this case, a lower-density or a faster beam may be a better description of 3C 449, and the ratio 16 : 6 of growth length to wavelength needed to fit the radio structure may be achieved by increasing the beam velocity (or density contrast) for a sheathed beam. The view that the beam in 3C 449 should be surrounded by a shear layer is consistent with the very short growth lengths of many reflection modes for the vortex-sheet beam model, so that even if these modes saturate at low amplitudes, their combined effect should be to broaden the edge of the beam. A very low density for the beam relative to the ambient medium may not be appropriate, however: numerical simulations of beam flows (e.g., Norman *et al.* 1984) find that such beams quickly develop a surrounding, lower-density, cocoon so that the beam is in contact with a low-density medium, and it is the cocoon that is in contact with the denser, external, medium.

The good, two-sided, C-type, symmetry of the radio structure of 3C 449 is a major problem for a pure Kelvin-Helmholtz instability model of the structure. Local conditions along the paths of the beams from the core of the galaxy should not produce phase-coherent structures on the two sides of the source. The perturbation driving the Kelvin-Helmholtz modes must therefore be applied to both beams coherently, presumably as perturbations at beam injection by the engine at the centre of the galaxy (UGC 12064). The observation that only a few wavelengths of oscillation appear in the structure of 3C 449 also argues that the perturbations are introduced at large amplitude, or that there is a strong non-linear mode competition between Kelvin-Helmholtz modes excited on the beam.

The apparent purity of the $n = 1$ mode causing the structure in 3C 449 is also a problem for the Kelvin-Helmholtz instability model (Birkinshaw 1984), since modes with growth length λ_e within about λ_e^{*2}/z of the minimum of the growth curve, λ_e^*, are amplified by the instability by within a factor $1/e$ of the maximum growth rate after the beam has travelled distance z. However, in 3C 449, it is clear that all the $n = 1$ modes that are present have wavelengths within $\Delta\lambda_0/\lambda_0 < 0.2$ of the mode that has grown. Since the jet is less than five wavelengths long, the mode appears to have been tuned more precisely than is possible according to Fig. 13. This problem is alleviated somewhat if the beam in 3C 449 is surrounded by a thick shear layer—such a layer in a low-density, fast, beam can increase the sharpness of a mode several-fold. This is not, of itself, sufficient to account for the sharpness of 3C 449's structure: it would require a propagation distance greater than $10\lambda_0^*$ for sufficient mode purity to be achieved for the clear structure of 3C 449 to be produced, whereas only two or three waves of the 'helical' structure of 3C 449 are seen on either side of the source. Therefore, if the Kelvin-Helmholtz model is to be adopted, strong mode competition must operate near the peak of the $n = 1$ resonance.

3.5.2. *Application to NGC 6251*

The spectacular jet of NGC 6251 was described in Sec. 1.2.3. It shows a number of wave-like structures. Within the first 40 arcsec, slowly–growing structures with apparent wavelength 5.7 and 9 arcsec can be identified although it is not known whether these correspond to sideways displacements of the jet ($n = 1$–like modes) or merely brightness enhancements and pinches ($n = 0$–like modes). At intermediate angular scales (120 to 240 arcsec), a rapidly–growing 31–arcsec oscillation which produces knots in the jet can be identified. Finally, on the largest scales (beyond 240 arcsec), the radius of the jet averages ≈ 10 arcsec and increases almost linearly, and the structure is dominated by a 143–arcsec oscillation which produces bulk displacements of the jet, and which has an almost linear growth with distance down the jet. In what follows, I will focus on the last, and best-defined, of the structural distortions of NGC 6251. In this region Perley *et al.* (1984a) estimate the flow to have a Mach number $\mathcal{M}_b \approx 13$, and that the beam is a factor $\gtrsim 3$ times less dense than the ambient medium, if the oscillations are interpreted as helical Kelvin-Helmholtz instabilities.

Hardee (1982, 1984) showed that on linearly expanding beams the Kelvin-Helmholtz instability does not grow exponentially, but that the local stability properties of the beam (that might be calculated using the local parameters of the flow and the local beam radius) may be used as global indicators of the stability of the flow. If the structural distortions of NGC 6251 are caused by the growth of a Kelvin-Helmholtz instability, then it is required that the beam should display a dominant $n = 1$ mode with $\lambda_0^* \sim 15R$. Perley *et al.*'s parameters for the beam are close to those for Fig. 13, although the lower beam density and higher speed may cause it to assume some of the (very similar) characteristics of the models in Figs 15 and 17. Then, just as for 3C 449, the dominant $n = 1$ mode for structures with scales $\gtrsim 10R$ is the ordinary mode, for which $\lambda_0^* \approx 27R$ and $\lambda_e^* \approx 10R$ if $\delta = 0$ and $\lambda_0^* \approx 79R$ and $\lambda_e^* \approx 42R$ if $\delta = 1$. A structure with projected wavelength $\lambda_0 \approx 15R$ cannot appear on this beam unless the apparent radio radius overestimates the radius of the flow.

At the large distance from the centre of NGC 6251 that the 143-arcsec oscillation is seen, the injected profile of the beam in NGC 6251 must have been modified by the growth of high-order modes. If the reflection modes saturate at amplitudes that cause weak shocks (Norman *et al.* 1984), then the modification of the beam profile on the small scale will have been severe, and the beam should have taken up a self-consistent form in which the further growth of small-scale modes is minimised. This argument would suggest that at any distance from the centre of the radio source, the dominant scale of structure that can be seen in the beam will be similar to the distance that the beam has propagated. This is certainly true for NGC 6251, and the question to be asked based on the shear layer analysis is then whether the dominant mode at wavelengths $\approx 15R$ has the correct ($n = 1$) symmetry to describe the oscillations in the position of the radio jet. According to Fig. 13, this is not possible unless the beam flowing through the radio jet is much narrower than the radio structure. The alternative, that the flow parameters estimated by Perley *et al.* (1984) are in error by a large factor, is perhaps more likely: simple results for the growth rates of Kelvin-Helmholtz instabilities were used to derive the flow parameters, and a shear layer could modify these rates substantially. Hardee & Norman (1989), from a slab beam simulation, also found that Perley *et al.*'s flow parameters were inconsistent with the generation of $n = 1$ Kelvin-Helmholtz modes of the correct wavelength, and suggested a smaller Mach number for the flow ($\mathcal{M}_b \sin\theta_{los} \sim 5$, where θ_{los} is the angle between the flow direction and the line of sight).

The one-sidedness of the jet in NGC 6251, and the lack of definition of the helical structure identified by Perley *et al.*, removes two of the arguments against the Kelvin-Helmholtz instability as a cause of the structure in this source, and the discussion above indicates that there is sufficient freedom in the parameters of the model to create agreement with the inferred $n = 1$ mode if the high-order modes are saturated at small amplitude. Further progress on applying the model to NGC 6251 awaits a calculation of the self-consistent structure of a beam that minimises the growth of the Kelvin-Helmholtz instabilities, and more precise data on the physical parameters of the flow and the ambient medium.

3.5.3. *Application to HH 34*

It is widely thought that galactic jets are dense (Section 2), so that their pattern of Kelvin-Holmholtz instabilities should more closely resemble Fig. 19 or 20 than Fig. 13 or 14. For almost all dense jets, at large wavelengths the growth rates increase as $\lambda_e \propto \lambda_0$, while at small wavelengths the growth rates are limited by the formation of a shear layer.

The flow pattern seen in HH 34 (Section 1.2.9) is not what we would predict based on these instability calculations. Rather what we are seeing resembles a 1-sided ejection of lumps of material, each with its own bow-shock. This corresponds more with a "bullet" than a "jet" model for the outflow, and Kelvin-Helmholtz instabilities are not appropriate for a discussion of the overall flow. Furthermore, the density of the outflowing material is such that radiative losses should be substantial—the equations of motion adopted for the analysis of the instability, which include the condition of the conservation of entropy are not appropriate in this case.

Instabilities will, however, be active in this flow: not only the Kelvin-Holmholtz instability, but also the Rayleigh-Taylor instability, both at the sides of the moving blobs of material and at their heads. These instabilities can be expected to act on very small linear scales, and give the moving blobs of gas an excited sheath, which may be the site of the [SII] and other line emission seen in optical images.

3.6. Summary and final considerations

The major theoretical difficulty in discussing astrophysical beams is that they are likely to be strongly turbulent—the Reynolds numbers of radio jets are $\sim 10^{28}$. An accurate description of jet structures, including bending and the propagation of large–scale waves, requires the use of a physically–consistent model for turbulence that permits reliable calculation of the Reynolds stresses.

Work so far has also neglected the effects of current sheets and field loops, where strong energy releases and anomalous transport coefficients can arise. Other entropy–generating processes have also been ignored. Chief among these is the transfer of energy from the flow to radiating particles, and hence the loss of energy through radiation. The thermal conductivity of the beam fluid may also be relevant if there is a significant transfer of heat by diffusive conduction.

Since the observed structures in jets are certainly of large amplitude, the theory of Kelvin–Helmholtz modes needs to be extended to describe their non–linear evolution. Only rudimentary ideas are available at present since the numerical results apply only to the longer–wavelength modes. These numerical simulations also suggest that the jet becomes sheathed by a hot, sheared cocoon which might protect the beam against Kelvin–Helmholtz instabilities. We need to calculate the structure of the (turbulent) flow pattern and sheathing layer that should be produced by the operation of short–wavelength instabilities on the beam.

For large–scale coherent structures to develop on the beam, the perturbing force must be coherent for times greater than the period of the structure. Since the dominant perturbations are most likely to be those encountered by the beam as it leaves a nozzle and is injected into the ambient medium, either a coherent perturbation is applied there, or mode competition between co–existing modes on the beam operates to set the dominant structure. The steadiness of the beam as it leaves the nozzle is also an issue, since theoretical investigations of the Kelvin–Helmholtz modes rely on the absence of significant variations in the injected flow. If such variations do exist, then it is likely that only full, three–dimensional numerical simulations will be capable of useful investigations of beam stability.

None of the instability calculations so far have taken account of the effects of structure in the external medium, except insofar as beam expansion has been included in Hardee's (1982, 1984) treatments. If the scale of variations in the beam parameters is much larger than the wavelengths and growth lengths of the instabilities, then the theory is changed only by the need to apply the dispersion relation locally. If the gradients of the beam parameters are large, then the effects of Kelvin–Helmholtz waves are unlikely to be important compared with the effects of shocks and other structures produced as the beam adjusts to its environment(e.g., Gouveia Dal Pino *et al.* 1995). Buoyancy effects on the dynamics of the beam in the stratified ambient atmosphere may also be important (Achterberg, 1982).

The present state of the theory of the Kelvin–Helmholtz instability for beams is that laminar, cylindrical, fluid flows are unstable for all beam velocities and densities unless the beam contains a strong, axial magnetic field, and that high–density flows are less unstable than low–density flows of the same beam velocity. Azimuthal magnetic fields, which can help to confine the beam, tend to destabilise the flow. Shear layers can either stabilize or destabilise the flow. The growth lengths of the instability are short, and so that it is likely to produce beam heating and turbulence on small scales (perhaps in a beam–sheath). On larger scales, where observable structural distortions of the flow may result, it has not yet been possible to find unambiguous predictions of the dominant modes because of uncertainties in the beam structure and the lack of information on the non–linear limit of the modes. A number of types of Kelvin–Helmholtz mode occur: the ordinary mode is the simple analogue of the instability as seen on a semi–infinite planar surface, while reflection modes arise from the partial trapping of magnetosonic waves inside the beam and resonances of these waves with the beam/ambient medium interface (over–reflection). The ordinary mode dominates the stability of a beam for low Mach number flows, whilst the reflection modes dominate for fast flows.

The Kelvin–Helmholtz model for the origin of structures in beams has achieved some successes, and such instabilities must influence the development of laminar beam flows, but at present little can be learned about any given flow through the application of the theory. If self–consistent results for the profiles of the jets and better estimates of the flow parameters were available, the present theory would allow strong statements about the stability of laminar flows to be made. Little work has been done so far on the development of coherent structures in turbulent flows.

References

Achterberg, A., 1982. A&A, 114, 233
Arnaud, K.A., Fabian, A.C., Eales, S.A., Jones, C. & Forman, W., 1984. MNRAS, 211, 981
Bailyn, C.D., Orosz, J.A., Girard, T.M., Jogee, S., della Valle, M., Begam, M.C., Fruchter, A.S., González, R., Ianna, P.A., Layden, A.C., Martins, D.H. & Smith, M., 1995. Nature, 374, 701
Bailyn, C.D., Orosz, J.A., McClintock, J.E. & Remillard, R.A., 1995. Nature, 378, 157
Bally, J. & Devine, D., 1994. ApJ, 428, L65
Balsara, D.S. & Norman, M.L., 1992. ApJ, 393, 631
Barsony, M., Scoville, N.Z. & Chandler, C.J., 1993. ApJ, 409, 275
Begelman, M.C., Rees, M.J. & Blandford, R.D., 1979. Nature, 279, 770
Benford, G., 1981. ApJ, 247, 792
Bicknell, G.V., 1984, In *Physics of energy transport in extragalactic radio sources*, eds. Bridle, A.H. & Eilek, J.A. (NRAO: Green Bank, WV) p. 229
Biretta, J.A. & Meisenheimer, K., 1993. In *Jets in Extragalactic Radio Sources*, 159; eds. Röser, H.-J. & Meisenheimer, K.; Springer, Berlin
Birkinshaw, M., 1984. MNRAS, 208, 887
Birkinshaw, M., 1991. MNRAS, 252, 505
Birkinshaw, M., Ho, P.T.P., Reid, M.J. & Zheng, X.W., 1995. In preparation
Birkinshaw, M. & Worrall, D.M., 1991. ApJ, 412, 568
Blake, G.M., 1972. MNRAS, 156, 67
Blandford, R.D. & Eichler, D., 1987. Phys. Rep., 154, 1
Blandford, R.D. & Icke, V., 1978. MNRAS, 185, 527
Blandford, R.D. & Rees, M.J., 1974. MNRAS, 169, 395
Blandford, R.D. & Pringle, J.E., 1976. MNRAS, 176, 443
Blondin, J.M., Fryxell, B.A. & Königl, A., 1990. ApJ, 360, 370
Blumen, W., Drazin, P.G. & Billings, D.F., 1975. J. Fluid Mech., 71, 305
Bodo, G., Rosner, R., Ferrari, A. & Knobloch, E., 1989. ApJ, 341, 631
Burbidge, G.R., 1956. ApJ, 124, 416
Burns, J.O., 1984. In *Physics of energy transport in extragalactic radio sources*, eds. Bridle, A.H. & Eilek, J.A. (NRAO: Green Bank, WV), p. 25
Burns, R.L. & Lovelace, R.V.E., 1982. Ap. J., 262, 87
Carilli, C.L., Perley, R.A. & Dreher, J.W., 1988. ApJ, 334, L73
Carilli, C.L., Bartel,N. & Diamond, P., 1994. AJ, 108, 64
Carilli, C.L., Perley, R.A., Leahy, J.P. & Dreher, J.W., 1991. ApJ, 383, 554
Chandrasekhar, S., 1961, *Hydrodynamic and Hydromagnetic Stability*, (Oxford University Press: Oxford)
Chernin, L.M. & Masson, C.R., 1995. ApJ, 443, 181
Cioffi, D.F. & Blondin, J.M., 1992. ApJ, 392, 458
Cioffi, D.F. & Jones, T.W., 1980. AJ, 85, 368
Clarke, D.A., Burns, J.O. & Feigelson, E.D., 1986. ApJ, 300, L41
Clarke, D.A., Norman, M.L. & Burns, J.O. 1986. ApJ, 311, L63
Clemmow, P.C. & Dougherty, J.P., 1969. *Electrodynamics of Particles and Plasmas*, (Addison-Wesley: Reading, MA)
Cohen, M.H. & Readhead, A.C.S., 1979. ApJ, 233, L101
Cohn, H., 1983. ApJ, 269, 500
Conway, R.G., Garrington, S.T., Perley, R.A. & Biretta, J.A., 1993. A&A, 267, 347
Curtis, H.D., 1918. Lick Obs. Publ., 13, 11
Davis, D.S., Mushotzky, R.F., Mulchaey, J.S., Worrall, D.M., Birkinshaw, M. & Burstein, D., 1995. ApJ, 444, 582

De Young, D.S., 1991. ApJ, 371, 69
De Young, D.S., 1984. In *Physics of energy transport in extragalactic radio sources*, eds. Bridle, A.H. & Eilek, J.A. (NRAO: Green Bank, WV), p. 202
Drazin, P.G. & Davey, H., 1977. J Fl. Mech., 82, 255
Drazin, P.G. & Reid, W.H., 1981. *Hydrodynamic Stability*, (Cambridge University Press: Cambridge)
Dreher, J.W., Carilli, C.L. & Perley, R.A., 1987. ApJ, 316, 611
Drury, L.O'C., 1983. Rep. Prog. Phys., 46, 973
Eilek, J.A., 1982. ApJ, 254, 472
Ershkovich, A.I., 1980. Sp. Sci. Rev., 25, 3
Fanaroff, B.L. & Riley, J.M., 1974. MNRAS, 167, 31P
Ferrari, A., Massaglia, S. & Trussoni, E., 1982. MNRAS, 198, 1065
Ferrari, A., Trussoni, E. & Zaninetti, L., 1978. A&A, 64, 43
Ferrari, A., Trussoni, E. & Zaninetti, L., 1979. A&A, 79, 190
Ferrari, A., Trussoni, E. & Zaninetti, L., 1980. MNRAS, 193, 469
Ferrari, A., Trussoni, E. & Zaninetti, L., 1981.MNRAS, 196, 1051
Fiedler, R.L., 1986. ApJ, 305, 100
Fiedler, R.L. & Jones, T., 1984. ApJ, 283, 532
Ford, H.C., Harms, R.J., Tsvetanov, Z.I., Hartig, G.F., Dressel, L.L., Kriss, G.A., Bohlin, R.C., Davidsen, A.F., Margon, B. & Kochhar, A.J,. 1994. ApJ, 435, L27
Forman, W. & Jones, C., 1982. ARAA, 20, 547
Fridlund, C.V.M. & Liseau, R., 1994. A&A, 292, 631
Gill, A.E., 1965. Phys. Fluids, 8, 1428
Goodman, A.A., Crutcher, R.C., Heiles, C., Myers, P.C. & Troland, T.H., 1989. ApJ, 338, L61
Gouveia Dal Pino, E.M. & Benz, W., 1993. ApJ, 410, 686
Gouveia Dal Pino, E.M., Birkinshaw, M. & Benz, W., 1995. ApJ, submitted
Hardee. P.E., 1979. ApJ, 234, 47
Hardee. P.E., 1981. ApJ, 250, L9
Hardee. P.E., 1982. ApJ, 257, 509
Hardee. P.E., 1983. ApJ, 269, 94
Hardee. P.E., 1984. ApJ, 287, 523
Hardee. P.E., 1986. ApJ, 303, 111
Hardee. P.E., 1987a. ApJ, 313, 607
Hardee. P.E., 1987b. ApJ, 318, 78
Hardee. P.E. & Clarke, D.A., 1992. ApJ, 400, L9
Hardee. P.E. & Norman, M.L., 1988. ApJ, 334, 70
Hardee, P.E. & Norman, M.L., 1989. ApJ, 342, 680
Hardee, P.E. & Norman, M.L., 1990. ApJ, 365, 134
Hardee, P.E., White, R.E., Norman, M.L., Cooper, M.A. & Clarke, D.A., 1992. ApJ, 387, 460
Harms, R.J., Ford, H.C., Tsvetanov, Z.I., Hartig, G.F., Dressel, L.L., Kriss, G.A., Bohlin, R.C., Davidsen, A.F., Margon, B. & Kochhar, A.J,. 1994. ApJ, 435, L35
Harris, D.E. & Stern, C.P., 1987. ApJ, 313, 136
Henriksen, R.N., 1987. ApJ, 314, 33
Hester, J. *et al.*, 1995. NASA press release, 6 June 1995
Hjellming, R.M. & Johnston, K.J., 1988. ApJ, 328, 600
Hjellming, R.M. & Rupen, M.P., 1995. Nature, 375, 464
Ho, C.M. & Huerre, P., 1984. Ann. Rev. Fluid Mech., 16, 365
Hughes, P.A. (ed.), 1991. *Beams and Jets in Astrophysics*, (Cambridge University Press: Cambridge)
Hughes, P.A., Aller, H.D. & Aller, M.F., 1985. ApJ, 298, 301
Jones, T.W. & O'Dell, S.L., 1977. ApJ, 214, 522
Junor, W. & Biretta, J.A., 1995. AJ, 109, 500
Kim, K.-T., Kronberg, P.P., Dewdney, P.E. & Landecker, T.L., 1986. In *Radio Continuum Processes in Clusters of Galaxies*, eds. O'Dea, C.P. & Uson, J.M. (NRAO: Green Bank)a

Kirk, J.G. 1994. In *Plasma Astrophysics*, Saas-Fee 24, eds. Benz, A.O. & Courvoisier, T.J.-L. (Springer-Verlag: Berlin)
Kochhar, R.K. & Trehan, S.K., 1988. MNRAS, 234, 123
Königl, A., 1980. Phys. Fluids, 23, 1083a
Laing, R.A., 1980. MNRAS, 193, 439
Laing, R.A., 1981. Ap. J., 248, 87
Laing, R.A., 1984. In *Physics of energy transport in extragalactic radio sources*, eds. Bridle, A.H. & Eilek, J.A. (NRAO: Green Bank, WV)
Laing, R.A. & Bridle, A.H., 1987. MNRAS, 228, 557
Landau, L.D. & Lifshitz, E.M., 1959. *Fluid Mechanics*; Pergamon Press
Leahy, J.P., 1984. MNRAS, 208, 323
Leahy, J.P., 1991. In *Beams and Jets in Astrophysics*; ed. Hughes, P.A. (Cambridge University Press: Cambridge)
Lerche, I. & Wiita, P.J., 1980. Ap. Sp. Sci., 68, 207
Linfield, R., 1985. ApJ, 295, 463
Loken, C., Burns, J.O., Clarke, D.A. & Norman, M.L., 1992. ApJ, 392, 54
Margon, B., 1984. ARAA, 22, 507
Misner, C.W., Thorne, K.S. & Wheeler, J.A., 1973. Gravitation, (Freeman: San Fransisco)
Morabito, D.D., Preston, R.A. & Jauncey, D.I., 1988. AJ, 95, 1037
Moriarty-Schieven, G.H. & Snell, R.L., 1988. ApJ, 332, 364
Mundt, R. & Fried, J., 1983. ApJ, 274, L83
Nepveu, M., 1982a. A&A, 105, 15
Nepveu, M., 1982b. A&A, 112, 223
Norman, M.L. & Hardee. P.E., 1988. ApJ, 334, 80
Norman, M.L., Smarr, L., Winkler, K.–H.A. & Smith, M.D., 1982. A&A, 113, 285
Norman, M.L., Winkler, K.–H.,A. & Smarr, L.L., 1983. In *Astrophysical Jets*, eds. Ferrari, A. & Pacholczyk, A.G. (Reidel: Dordrecht, Holland), p. 227.
Norman, M.L., Winkler, K–H.A. & Smarr, L., 1984. In *Physics of energy transport in extragalactic radio sources*, eds. Bridle, A.H. & Eilek, J.A. (NRAO: Green Bank, WV), p. 150
O'Dea, C.P. & Owen, F.N., 1986. ApJ, 301, 841
Owen, F.N., Hardee, P.E. & Cornwell, T.J., 1989. ApJ, 340, 698
Payne, D.G. & Cohn, H., 1985. ApJ, 291, 655
Pearson, T.J., Unwin, S.C., Cohen, M.H., Linfield, R.P., Readhead, A.C.S., Seielstad, G.A., Simon, R.S. & Walker, R.C., 1981. Nature, 290, 365
Perley, R.A., Bridle, A.H. & Willis, A.G., 1984a. ApJS, 54, 291
Perley, R.A., Dreher, J.W. & Cowan, J., 1984b. ApJ, 285, L35
Perley, R.A., Willis, A.G. & Scott, J.S., 1979. Nature, 281, 437
Ray, T.P., 1981. MNRAS, 196, 195
Ray, T.P., 1982. MNRAS, 198, 617
Ray, T.P. & Ershkovich, A.I., 1983. MNRAS, 204, 821
Rees, M.J., 1971. Nature, 229, 312 and 510
Reid, M.J., Biretta, J.A., Junor, W., Muxlow, T.W.B. & Spencer, R.E., 1989. ApJ, 336, 112
Reipurth, B., Bally, J., Graham, J.A., Lane, A.P. & Zealey, W.J., 1986. A&A, 164, 51
Roberts, B., 1987. ApJ, 318, 590
Roberts, F.A., Dimotakis, P.E. & Roshko, A., 1982. In *Album of Fluid Motions*, ed, A. Van Dyke, (Parabolic Press: Stanford, California)
Rodriguez, L.F., Canto, J., Torrelles, J.M. & Ho, P.T.P., 1986. ApJ, 301, L25
Roy Choudhury, S. & Lovelace, R.V.E., 1984. ApJ, 283, 331
Roy Choudhury, S. & Lovelace, R.V.E., 1986. ApJ, 302, 188
Rudnick, L. & Edgar, B.K., 1984. ApJ, 279, 74
Sarazin, C., 1986. Rev. Mod. Phys., 58, 1
Scheuer, P.A.G., 1974. MNRAS, 166, 513
Seward, F., Grindlay, J., Seaquist, E. & Gilmore, W., 1980. Nature, 287, 806
Snell, R.L. & Schloerb, F.P., 1985. ApJ, 295, 490
Spitzer, L., 1962. Physics of fully ionized gases, (Interscience: New York)

Stewart, P., 1971. Ap. Sp. Sci., 14, 261
Stocke, J.T., Hartigan, P.M., Strom, S.E., Strom, K.M., Anderson, E.R., Hartmann, L.W. & Kenyon, S.J., 1988. ApJS, 68, 229
Synge, J.L., 1957. *The Relativistic Gas* (North–Holland Publ. Co.: Amsterdam)
Thomson, R.C., Mackay, C.D. & Wright, A.E., 1993. Nature, 365, 133
Trussoni, E., Massaglia, S., Bodo, G. & Ferrari, A., 1988. MNRAS, 234, 539
Turland, B.D. & Scheuer, P.A.G., 1976. MNRAS, 176, 421
Vermeulen, R.C., Schilizzi, R.T., Spencer, R.E., Romney, J.D. & Fejes, I., 1993. A&A, 270, 177
Waggett, P.C., Warner, P.J. & Baldwin, J.E., 1977. MNRAS, 181, 465
Watson, M.G., Willingale, R., Grindlay, J.E. & Seward, F.D., 1983. ApJ, 273, 688
Wiita, P.J. & Norman, M.L., 1992. ApJ, 385, 478
Wiita, P.J., Rosen, A. & Norman, M.L., 1990. ApJ, 350, 545
Williams, A.G., 1991. In *Beams and Jets in Astrophysics*, (Cambridge University Press: Cambridge)
Williams, A.G. & Gull, S.F., 1984. Nature, 310, 33
Williams, A.G. & Gull, S.F., 1985. Nature, 313, 34
Wirth, A., Smarr, L. & Gallagher, J.S., 1982. AJ, 87, 602
Worrall, D.M. & Birkinshaw, M., 1994. ApJ, 427, 134
Zaninetti, L., 1986a. A&A, 156, 194
Zaninetti, L., 1986b. A&A, 160, 135
Zaninetti, L. & Van Horn, H.M., 1988. A&A, 189, 45